PROCESSING OF BI-2212 HIGH TEMPERATURE SUPERCONDUCTING WIRES

BACHELOR THESIS

by

Christopher Dörrer

Supervisor at CERN

Christian Scheuerlein M.Sc.

Supervisor at Hochschule Esslingen

Prof. Dr.-Ing. Ralph Schmidt

Hochschule Esslingen
University of Applied Sciences

CERN

Faculty of Mechanical Engineering

2015

ABSTRACT

Bi-2212 high temperature superconductors can be used for producing very high magnetic fields. They are studied at CERN for potential use in accelerator magnets. The powder-in-tube wires are produced by inserting Bi-2212 particles into a Ag matrix. In order to transport high supercurrents the Bi-2212 needs to be melted during a processing heat treatment in a process gas containing oxygen.

For the processing of Bi-2212 wires a 100 bar overpressure furnace has been designed at CERN. The first part of this thesis describes the setting up of a high pressure gas supply system and its installation. To ensure the safe operation of the overpressure furnace the high pressure reaction cell has been pressure tested up to 250 bar. A LabVIEW program was developed in order to control the pressure during the heat treatment and to record the furnace temperature.

The oxygen partial pressure in the process gas influences the phase sequence and the Bi-2212 melting temperature. The phase changes during the processing of Bi-2212 wires at different oxygen partial pressures have been studied by means of *in situ* synchrotron X-ray diffraction experiments, performed at the high energy scattering beamline ID15B at the European Synchrotron.

In the second part of this thesis the results of the analysis of more than 1000 diffractograms that were acquired during different heat cycles are presented. The temperature dependent variation of the Ag lattice constants of the Ag matrix of the wires has been determined as a cross-check of the temperature that was measured during the experiments with a thermocouple. In this way important temperature uncertainties have been detected for one type of thermocouples.

ACKNOWLEDGEMENT

I would like to express my gratitude towards all people who accompanied and supported me throughout this project.

Special thanks go to Christian Scheuerlein and Ralph Schmidt for their supervision and provision of necessary information regarding the project.

During the experimental beamtime at the ESRF it was a pleasure to cooperate with Jerome Andrieux and Julian Kadar.

I would like to thank the LabVIEW team especially Odd Andreassen and Adriaan Rijllart for their support in programming and the good advice in selecting suitable hardware components.

I want to thank Didier Gonnard for the performance of the high pressure test of the pressure reaction cell.

My thanks and appreciations also go to my colleagues, Marina Garcia Gonzales who was providing the migrographs, Roger Bjoerstad for his assistance with MATLAB and Jonathan Speed for the grammatical cross checking of this thesis.

TABLE OF CONTENTS

LIST OF FIGURES

LIST OF TABLES

NOMENCLATURE

Acronyms and Abbreviations

Ag	Silver
ASC	Applied Superconductivity Center
BSCCO	Bismuth strontium calcium copper oxide
CeO_2	Cerium dioxide
CERN	French: Conseil Européen pour la Recherche Nucléaire
cRIO	Compact reconfigurable input output
ESRF	European Synchrotron Radiation Facility
FCC	Future circular collider
GmbH	German: Gesellschaft mit beschränkter Haftung
HT	Heat treatment
HTS	High temperature superconductor
LHC	Large Hadron Collider
Mg	Magnesium
MRI	Magnetic resonance imaging
MSC	Magnets, Superconductors and Cryostats
NHMFL	National High Magnetic Field Laboratory
NI	National Instruments
NIST	National Institute of Standards and Technology
NMR	Nuclear magnetic resonance
NSC	Nexans SuperConductors
OP	Overpressure
OST	Oxford Superconducting Technology
PIT	Powder-in-tube
RT	Room temperature
SS	Stainless steel
TE	Technology Department
XRD	X-ray diffraction

Variables

a	Lattice constant
c	Speed of light
d	Distance of two parallel lattice planes
E	Energy
h	Planck constant
H	Magnetic field

h,k,l	Miller indices
H_C	Critical magnetic field
J	Current density
J_C	Critical current density
λ	Beam wave length
p	Pressure
p_{atm}	Atmospheric pressure
Q	Ratio of distance of two parallel lattice planes to $2\times\pi$
$\dot{Q}$	Heat flow
R	Electrical resistance
r	Radius of diffraction ring
Rz	Average surface roughness
S_b	Safety factor against break
S_f	Safety factor against plasticity
σ_b	Ultimate stress
σ_f	Yield stress
σ_v	Von Mises stress
T	Temperature
T_C	Critical temperature
ϑ	Temperature in degrees Celsius
θ	angle between X-ray and lattice plane
U	Voltage
u	Diameter ratio
wt%	Percentage by weight
x	Sample-to-detector distance

Units

°C	Degrees Celsius
Å	Angstrom
eV	Electronvolt
h	Hour
HRB	Hardness Brinell
HRV	Hardness Vickers
K	Kelvin
m	Metre
min	Minutes
N	Newton
Pa	Pascal
s	Second

T	Tesla
V	Volts
W	Watt

1 Introduction

About CERN and the technology department

At CERN, the European Organization for Nuclear Research (French: Conseil Européen pour la Recherche Nucléaire), physicists and engineers are probing the fundamental structure of the universe. They use the world's largest and most complex scientific instruments to study the basic constituents of matter – the fundamental particles. The particles are made to collide together at close to the speed of light. The process gives the physicists clues about how the particles interact, and provides insights into the fundamental laws of nature.

The instruments used at CERN are purpose-built particle accelerators and detectors. Accelerators boost beams of particles to high energies before the beams are made to collide with each other or with stationary targets. Detectors observe and record the results of these collisions.

Founded in 1954, the CERN laboratory sits astride the Franco-Swiss border near Geneva. It was one of Europe's first joint ventures and now has 21 member states. [1]

Since the main studies at CERN deal with fundamental constituents of matter it is also called the European Laboratory for Particle Physics. However pure physics is not the only work that is done at CERN. There are also other tasks to handle that the organisation has grouped in eight major departments which are:

- Beams
- Engineering
- Finance, Procurement and Knowledge Transfer
- General Infrastructure Services
- Human Resources
- Information Technology
- Physics
- Technology

The present studies were implemented in the technology department (TE), whose organisation [2] is shown in Figure 1, in the Magnets, Superconductors and Cryostats (MSC) group. The group concerns itself with the design of superconducting and normal conducting magnets for the CERN accelerator complex. Furthermore it is responsible for developing associated technologies such as superconductors, insulation and polymers and magnetic measurements [3].

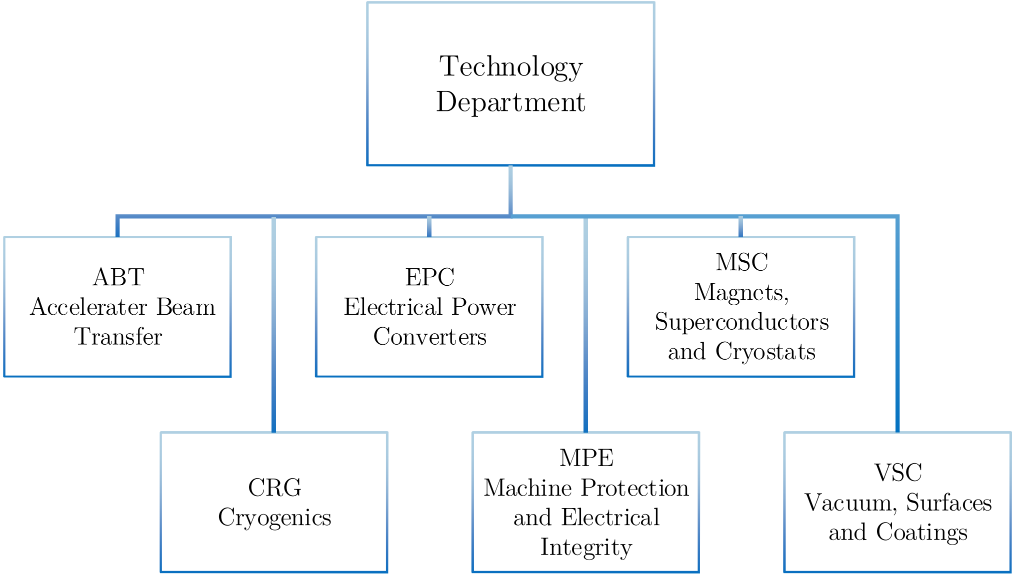

Figure 1. Organisation of the technology department [2].

The Large Hadron Collider (LHC)

The most famous, and with 27 km [4] size biggest accelerator at CERN, is the LHC. The LHC accelerates bunches of hadrons mostly protons or lead nuclei in two separate beam pipes in the opposite direction, shown in a cross sectional view [5] in Figure 2. During operation the particles orbit the whole accelerator path about 11 000 times per second in an ultra-high vacuum, up to 10^{-14} bar [6].

The collisions happen in one of four points where the two beams cross each other. In order to see what happens when the particles collide, each crossing point includes an experiment with a particle detector. These are the main experiments at the LHC called ALICE, LHCb, ATLAS and CMS. Within every experiment it is possible to get different information out of the collision due to a different experimental setup. ALICE for example shall give more information about what happens right after a particle collision.

To be able to create such collisions the LHC accelerates the particles to a very high energy, up to 14 TeV [6]. At this energy it is necessary to have a very strong magnetic field that holds the particles on their track, therefore the use of superconducting magnets becomes essential. This requires cooling them to 1.9 K [6] which is done by using liquid helium. At this temperature the niobium titanium superconducting coils of the dipole magnets produce a magnetic field at maximum power of about 8 T [6].

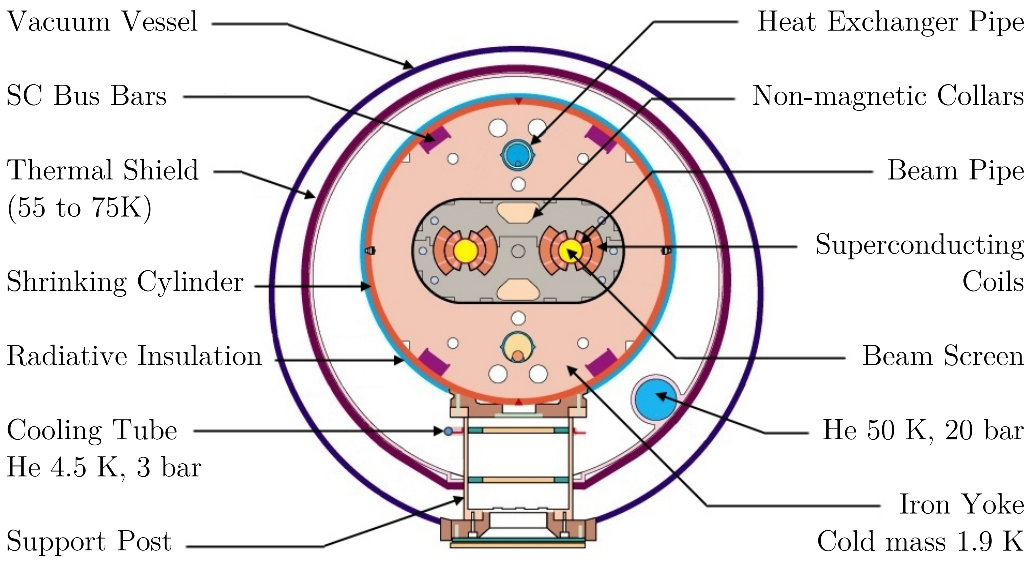

Figure 2. Cross section of the LHC dipole [4].

The greatest discovery with the LHC was in 2012 where physicists found a new particle whose properties match with those of the Higgs Boson. Although the detectors ATLAS and CMS have shown several of these Higgs events, measurements need to be completed before the found particle can be fully verified as the Higgs Boson.

Future CERN projects and need of very high field magnets

For producing even more collisions at higher energies CERN is already planning what will come after the LHC. One project that could be realised is given below. In the ongoing design study of the so called ‘Future Circular Collider’ (FCC) scientists examine the possibility of building an 80 km tunnel in the Geneva area. Depending on the energies which shall be finally achieved, magnetic flux densities of up to 20 T [7] could be needed. Such high fields can be reached using high temperature superconductive coils. However, lots of developments will be necessary before these can be manufactured in the required form.

Processing of Bi-2212 high temperature superconductors (HTS)

Bi-2212 is one candidate of HTS that is being considered for use in the construction of very high field accelerator magnets. This thesis describes two subjects related to the processing of such Bi-2212 high temperature superconducting wires.

The first part of this thesis is about the development and commissioning of an overpressure (OP) furnace for the processing of Bi-2212 wires. In the second part a synchrotron X-ray diffraction (XRD) experiment for the study of the influence of the oxygen partial pressure (p_{O2}) on the phase changes in Bi-2212 wires during the processing is described. The XRD data that has been acquired *in situ* during the heat treatment (HT) of Bi-2212 wires at different p_{O2} is analysed.

2 Basics

2.1 Superconductivity

The quantum mechanical phenomenon of a material that causes a complete loss of its electrical resistance when going below a critical temperature is called superconductivity. For most superconductors this critical temperature is very low, so they have to be cooled with liquid helium. However, the temperature is not the only criteria that must be fulfilled to achieve the superconductive state. Also, the current and the applied magnetic field are limited to a maximum value depending on the respective material [8]. Plotting these requirements in three axes they form a critical surface [9], shown in Figure 3, under which the material is superconductive. If this surface is exceeded the resistance of the conductor will increase rapidly.

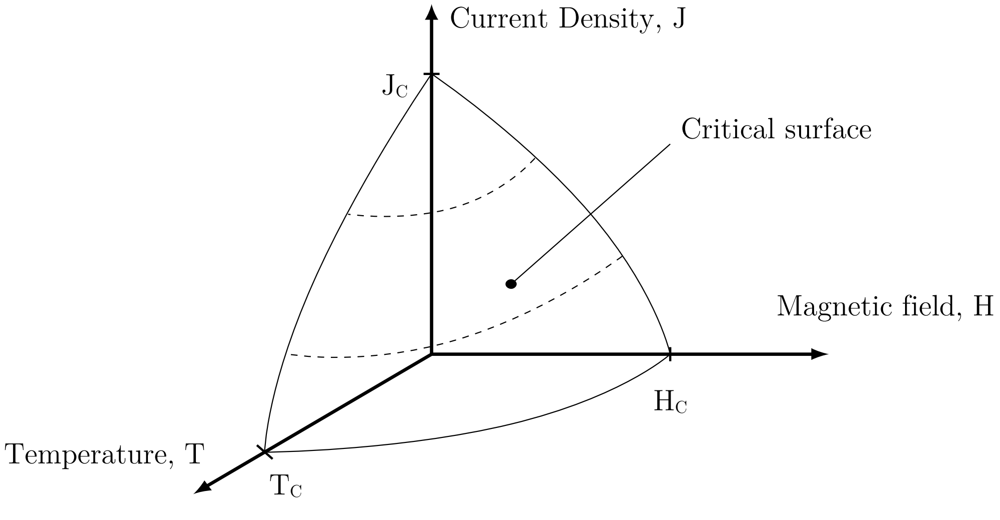

Figure 3. Critical surface for superconducting state [9].

There are some superconductors where the critical temperature is significantly higher than in others. These are called HTS. HTS mostly consist of brittle ceramic composites, which makes it difficult to process them. But there are also a lot of advantages that come with the use of HTS. Due to the high critical temperature, cooling can be done more cheaply using liquid nitrogen. Also, a very high current density means that the quotient of the critical current and the superconducting area is achievable at high magnetic fields.

This makes it interesting to use HTS for many applications. The mentioned future CERN projects, where it is necessary to provide very high fields for more powerful accelerators, is only one of them. Also, in the medical industry, for instance, HTS are used for nuclear magnetic resonance (NMR) and magnetic resonance imaging (MRI) [10] where they achieve better imaging quality due to higher magnetic fields.

2.2 Bi-2212 superconducting wires

Wherever it is necessary to create very high magnetic fields conventionally used superconductors such as niobium titanium and niobium tin cannot be used because of their operating limitations in very high applied magnetic fields. One solution comes with the use of magnetic coils made out of $Bi_2Sr_2CaCuO_{8-x}$ (Bi-2212) wires. This HTS belongs to the BSCCO superconducting family that all consist of bismuth strontium calcium copper oxide.

The Bi-2212 wires are unique in that they can carry high critical current densities in strong magnetic fields. Another advantage is that Bi-2212 is the only HTS that can be produced as a round wire [11]. This makes them very interesting for the aforementioned CERN upgrades because many techniques from other, previously used, superconducting wires will be applicable. The critical temperature of Bi-2212 is about 95 K [12] but the critical field and the critical current increase with reducing temperature.

To create wires that are suitable for making magnetic coils the brittle Bi-2212 material cannot be used directly. Therefore, a round wire is made using the powder in tube (PIT) process which is already widely used for other superconducting wires. This technique is based on the use of a ductile matrix in which the superconductor is inserted in powder form.

The created Bi-2212 precursor is filled in a single silver tube which is going to be drawn to a monochore wire. Many of these are put together to form a sub-element where they are deformed again. Then several sub-elements, plus an additional silver stack in the middle, are stacked in an outer sheath where it will be drawn to its final diameter.

A metallographic cross section of such a manufactured Bi-2212 round wire is shown in Figure 4. The wire with billet number pmm 100610 has been produced by Oxford Superconducting Technology (OST) using a precursor powder that was manufactured by Nexans SuperConductors GmbH (NSC). It consists of 18 hexagonal stacked sub-elements. Each sub-element contains 37 filaments, so there are 18×37=666 filaments in total in one wire. The wire was drawn to an outer diameter of 0.8 mm whereby the filaments diameter is approximately 15 µm. To improve the mechanical strength of the wire the outer sheath contains 0.2 wt% magnesium [13].

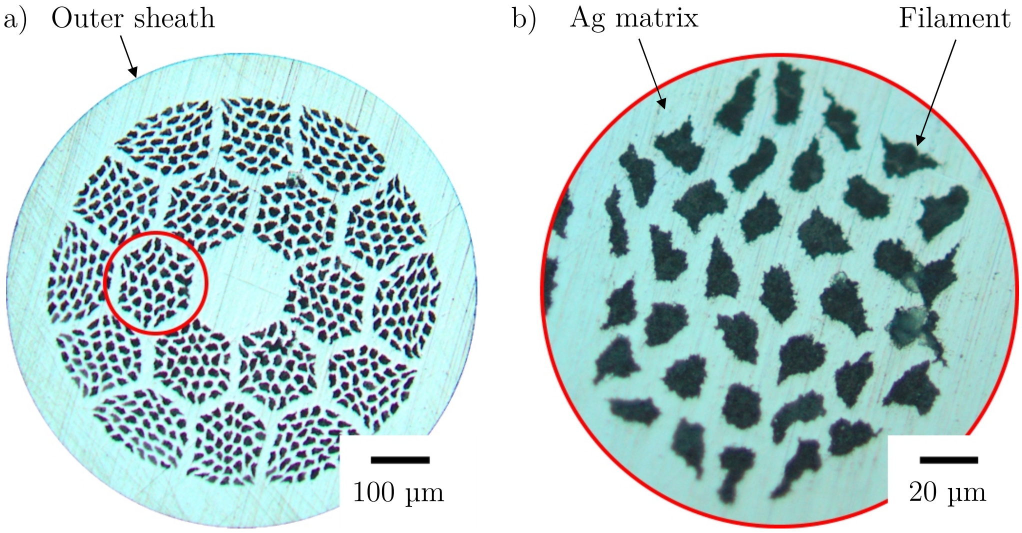

Figure 4. a) Cross section of a wire before any HT. b) Sub-element with its single filaments in the Ag matrix.

As the next processing step the present wire would be brought to its needed shape, for example a coil, before it is heated up, in order to melt the powder inside the silver matrix. Once the wire has been heat-treated it should not be deformed again because of the then brittle filaments. An oxygen supply in the process gas during the HT is essential to re-form the superconducting Bi-2212 phase during cool down of the wire [13]. This means that the matrix has to be permeable to oxygen. In addition to that the matrix has to provide good electrical and thermal conductivity properties for protection in case of a sudden loss of superconductivity, known as quench. Because of those reasons silver is used as matrix for Bi-2212 wires.

Recent studies show that the maximum current density achievable in the superconducting wire increases when the HT is done at higher p_{O2} because OP processing strongly reduces porosity of the wire [11]. A typical HT for the processing of Bi-2212 wires is shown in Figure 5 [14].

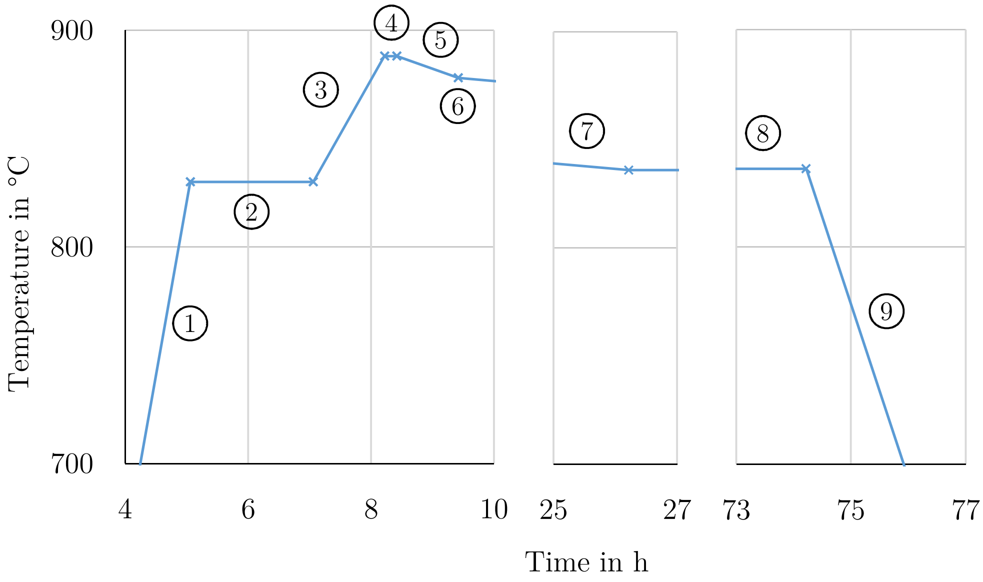

Figure 5. Typical HT for the processing of a Bi-2212 wire [14].

The temperature ramp rates and plateaus are listed in Table 1. The HT is divided into segments which simplifies the coding of the temperature curve. The odd numbered segments are used for linear temperature slopes while the even numbered segment are reserved for constant temperature plateaus.

Table 1. Single segments for the HT.

Segment	*1*	*2*	*3*	*4*	*5*	*6*	*7*	*8*	*9*
Ramp rate in °C/h	160	-	50	-	10	-	2.5	-	80
Temperature plateau in °C	-	830	-	888	-	878	-	836	-
Duration of pause in h	-	2	-	0.2	-	0	-	48	-

2.3 Furnaces for processing of superconductors

For the implementation of the HT for superconductors different types of furnaces exist. Depending on the exact purpose they vary in size and composition. Shown below are some selected furnaces at CERN. Figure 6 shows two tube furnaces that are used for processing of Niobium-tin (Nb_3Sn) wires.

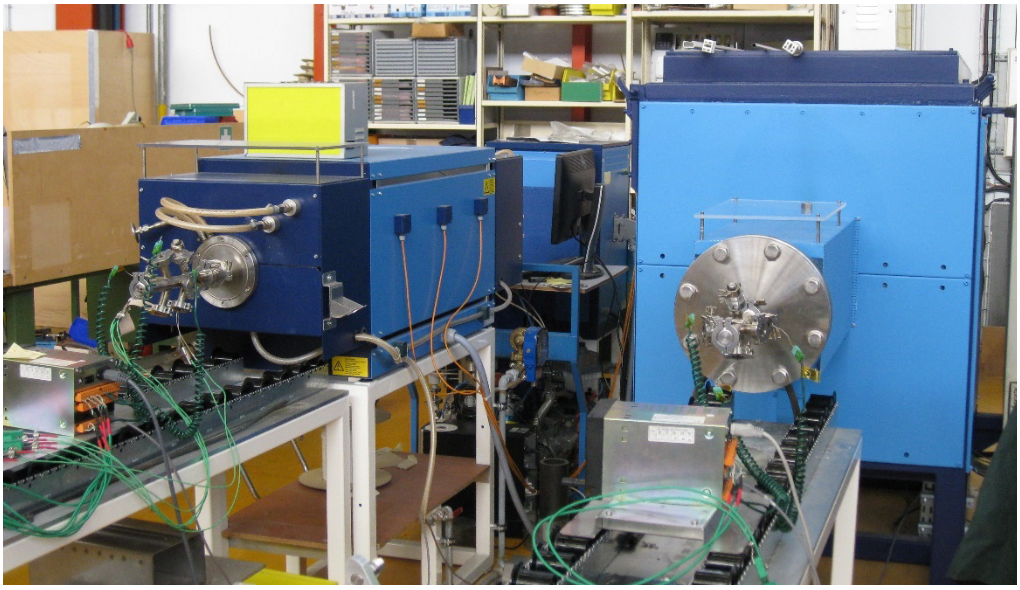

Figure 6. Tube furnaces for processing of superconducting wires at CERN, B163.

A hood type furnace and a tube furnace for processing of superconducting coils are shown in Figure 7.

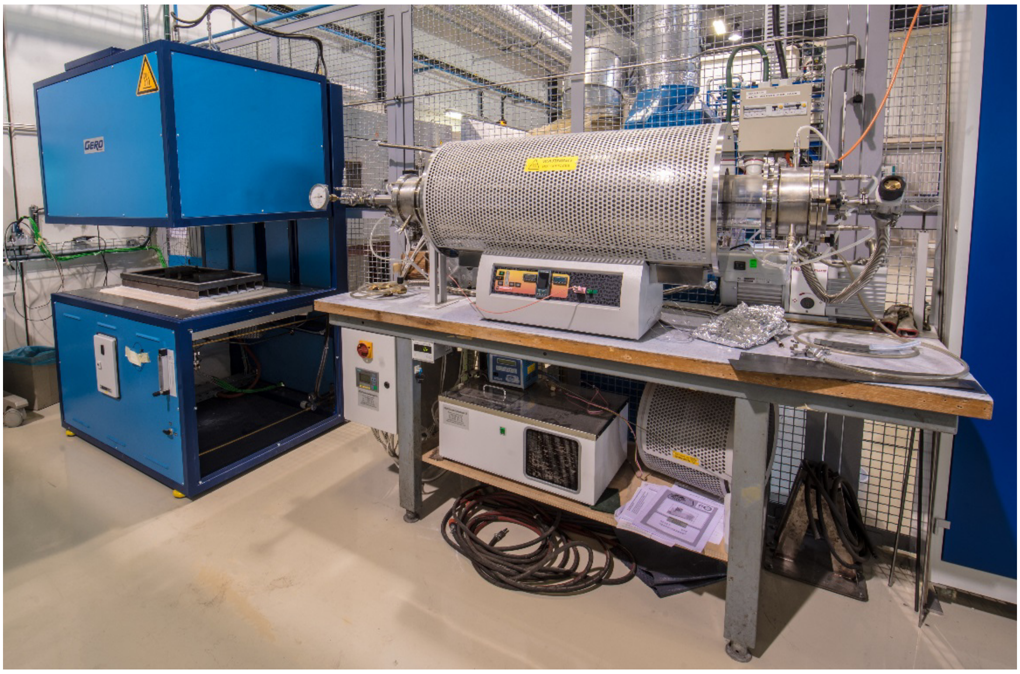

Figure 7. Hood type furnace on the left and a tube furnace on the right hand side at CERN, B927.

2.4 Temperature and pressure measurement

Thermocouples

Thermocouples are often used for industrial high accuracy measurements. Their measuring principle, shown in Figure 8, is based on the Seebeck effect whereby a temperature gradient between a junction point of two different materials and a reference point forces a separation of charge that can be measured as a voltage, U. Every voltage measured equates to a corresponding temperature that depends on the used material couple.

In addition, it is also necessary to know the temperature of the reference point which is mostly done by using a resistive thermometer. The absolute temperature to be measured is then calculated by the sum of both temperatures.

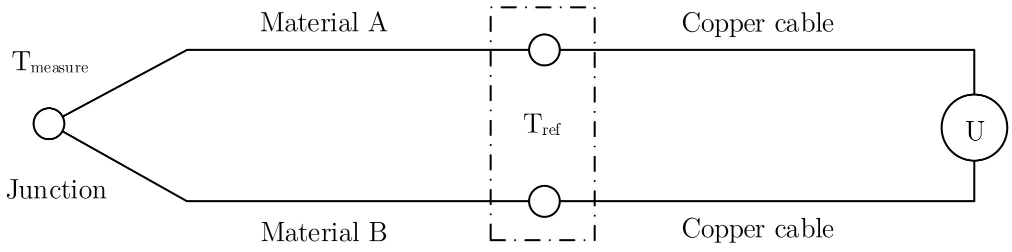

Figure 8. Principle of temperature measurement using a thermocouple.

Generally, the Seebeck effect appears at many conductive couples. But, of course, not all of them find an industrial use. In order to cover meaningful applications industry provides different material couples which vary in cost and accuracy. The calibrations N and S, for instance, are suitable for high temperature measurements. Their maximal errors are standardised in DIN EN 60584-2 which is shown in extracts in Table 2.

Table 2. Temperature errors of some thermocouples according to DIN EN 60584-2.

Thermocouple	*Temperature range in °C*	*Temperature error in °C*
Type S, R	0 to 1100	± 1.0
	1100 to 1600	$\pm [1 + 0.003 \cdot (\vartheta - 1100)]$
Type N, K	− 40 to 375	± 1.5
	375 to 1000	$\pm 0.004 \cdot (\vartheta)$

At high temperatures it is common to protect the junction point and the wires from the measuring atmosphere to prevent it from corrosive malfunction. Thus, the endangered hot areas are shielded through a metallic sheath.

Piezoresistive pressure meters

There are many different ways to measure the absolute pressures of fluids. One of them uses the principle of the piezoresistive effect that describes a resistive change of a material when it is mechanically deformed.

Instead of using one straight conductor, strain gauges are often used to intensify the sensitivity especially for small strains. Those consist mostly of a flexible insolating film on which a thin conductor is integrated in a zig-zag shape as shown in Figure 9 a). This pattern allows high changes in resistance at small areas. The resistance that can be measured between the solder pads increases with extension and decreases with compression.

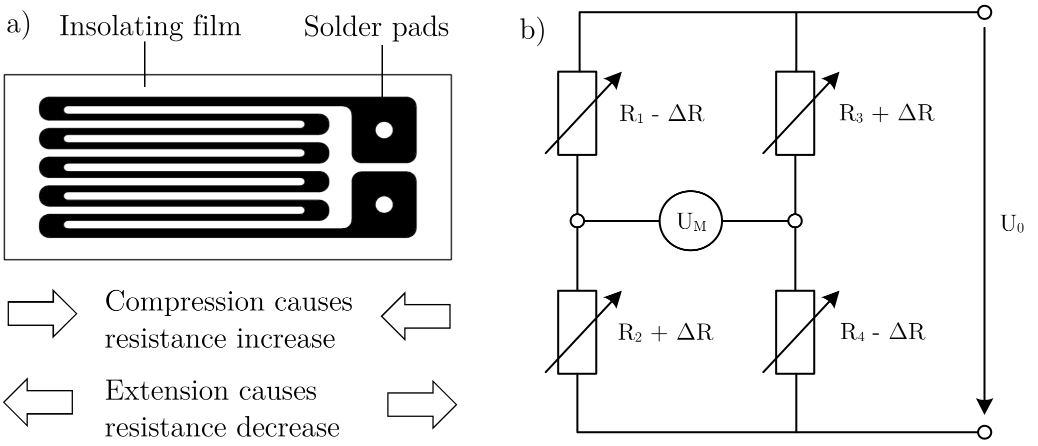

Figure 9. a) Structure of a foil strain gauge. b) Wheatstone bridge with for strain gauges.

Resistive pressure meters usually use such strain gauges within a Wheatstone bridge shown in Figure 9 b). The four strain gauges are attached onto a flexible membrane which constitutes the pressure sensor. Now, when a pressure is applied on this sensor, the strain gauges will be either elongated or compressed depending on their position on the membrane. In the Wheatstone bridge this can then be measured as a voltage U_M. The higher the pressure the higher the voltage. The voltage corresponds to a characteristic pressure that depends on the exact model.

2.5 X-ray diffraction

According to Bragg's law (see Equation 2.1) the distance between two lattice planes of a material referred to d-spacing can be calculated when measuring the angle of the diffracted beam at known wavelength.

$$n \cdot \lambda = 2 \cdot d \cdot sin(\theta) \qquad 2.1$$

Where

n	is a natural number
λ	is the wavelength of the incident beam
d	is the distance of two parallel lattice planes
θ	is the angle between X-ray and lattice plane

The schematic view of an experimental setup for XRD measurements in transmission geometry is shown in Figure 10. The experiment in transmission geometry uses a two dimensional detector to acquire an image of the X-rays that are diffracted in the sample. The very intense non-diffracted part of the beam is going to be is absorbed by a beamstop in order not to damage the detector.

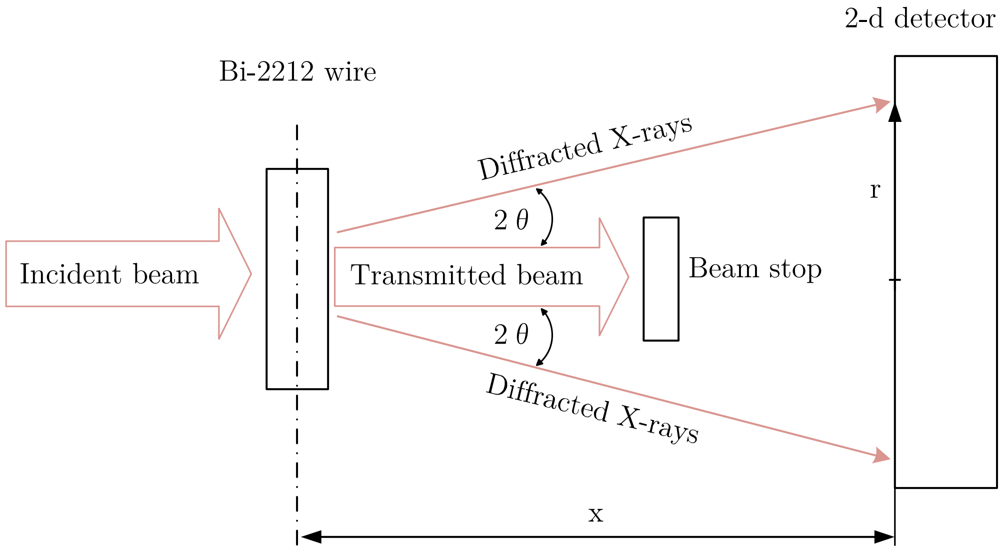

Figure 10. Schematic view of synchrotron XRD at a Bi-2212 wire.

A diffraction ring with the radius r is recorded for a polycrystalline sample with random crystallite orientation, while the diffraction pattern of a single crystal appears at distinct diffraction spots.

The geometric arrangement of Figure 10 can be described by Equation 2.2.

$$tan(2\theta) = \frac{r}{x} \tag{2.2}$$

Where

r	is the radius of the diffraction ring
x	is the sample-to-detector distance

The lattice constant of a cubic material structure can be calculated from the d-spacing and the respective Miller indices as shown in Equation 2.3.

$$a = d \cdot \sqrt{h^2 + k^2 + l^2} \tag{2.3}$$

Where

h, k, l	are the Miller indices of the Bragg plane

Synchrotron XRD experiments can be performed, for example, at the European Synchrotron Radiation Facility (ESRF). The ESRF in Grenoble offers scientists the possibility to use synchrotron radiation from an 844 m circumference electron accelerator. In the tangential arranged beamlines where the synchrotron radiation is emitted users can perform several experiments like XRD or micro computer tomography. The performed XRD experiments that are later described in this thesis have been performed at the high energy scattering beamline ID15B [15].

The different phases present in the sample can be identified by comparing the d-spacing of the different intensity peaks of the acquired diffractogram with reference diffractograms. The very high flux of high energy photons provided through the beamline ID15B enables the acquisition of diffractograms in transmission geometry within seconds. This allows time resolved *in situ* studies of the phase changes during the melt processing of Bi-2212 wires.

3 OP furnace for processing of Bi-2212 wires

3.1 Initial status of the furnace

An existing tube furnace at CERN can be used for HT of Bi-2212 wires in air at ambient pressures. The furnace, produced by Severn Furnace Limited (SFL), is shown in Figure 11. The tube of the furnace has an outer diameter of 200 mm and is 460 mm long. Its inner tube diameter is 50 mm. The furnace uses a one phase power supply of 230 V. At a maximum power of 1.5 kW the furnace reaches a temperature of 1200 °C.

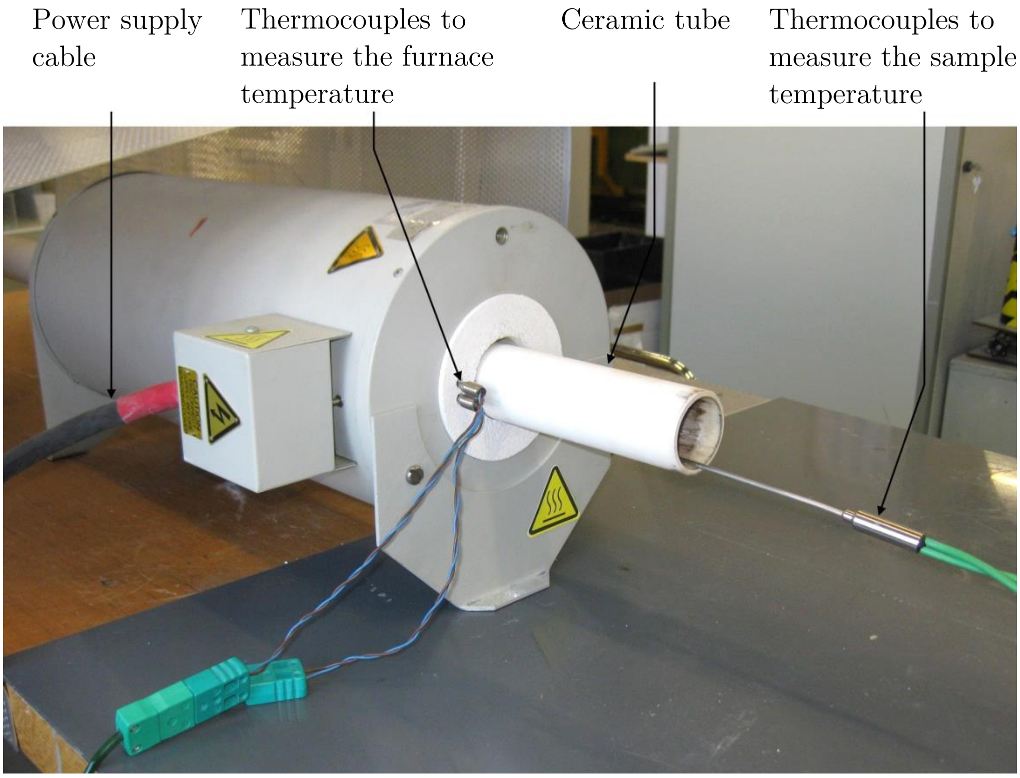

Figure 11. Tube furnace in operating state with thermocouples inside.

The Bi-2212 samples are placed inside the tube of the furnace by means of a sample holder whose temperature is measured with two thermocouples that are placed in a metallic sheath (see Figure 12). The sample holder was designed in former studies [16]. It is mounted on the sheath of the thermocouples and holds up to six samples positioned in machined slots symmetrical about the axis. A casing that has also previously been designed fits on the outer diameter of the sample holder and prevents the samples falling out.

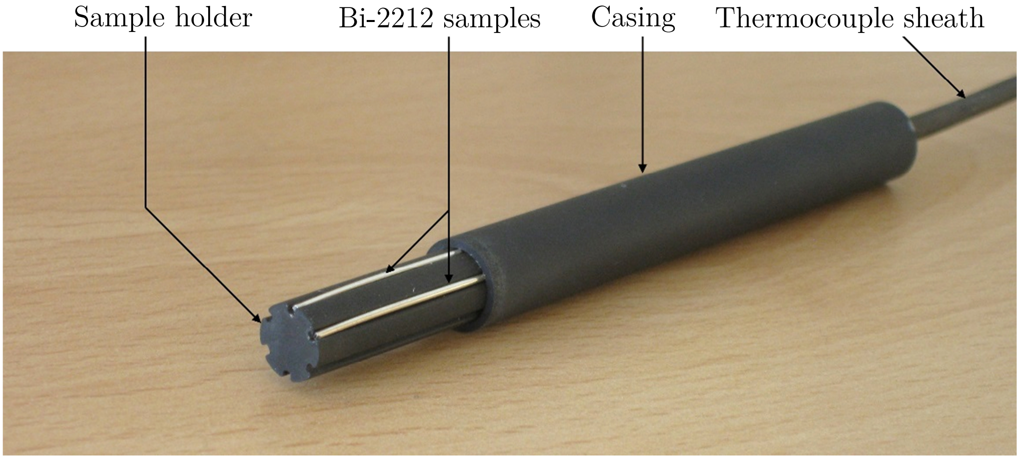

Figure 12. Sample holder with Bi-2212 wires and sheath of the thermocouples.

The measured sample temperature of one thermocouple is used to control the input power of the furnace via a Honeywell UDC 3000 universal digital controller. The other thermocouple is used for temperature recording. Before starting this project the temperature could only be recorded with an analogue flatbed chart recorder.

In order to implement an upgrade of the existing tube furnace that allows the performance of high pressure HT of Bi-2212 wires a high pressure gas supply system shall be installed. For that a high pressure cell made out of Hastelloy X-750 was designed and produced [16]. The dimensions of this tube were: an outer diameter of 30 mm, an inner diameter of 12 mm and a length of 700 mm. Also a pressure control system had been selected.

3.2 Present tasks for the OP furnace upgrade

For the ongoing upgrade of the tube furnace for OP processing the design of the high pressure gas supply system needed to be finished. The already delivered components such as the Hastelloy X-750 high pressure cell, a pressure controller and a leak valve had to be connected. Afterwards the entire high pressure set-up had to be tested at high pressure.

A LabVIEW program needed to be developed for the control and continuous acquisition of the pressure inside the high pressure cell. The operating pressure shall reach up to 100 bar using industrial air. For the system it also had to be considered that it has to resist the high temperatures, up to 900 °C, that occur during the HT.

Furthermore, the analogue temperature flatbed chart recorder required replacing. Instead, that thermocouple had to be connected to a digital data acquisition instrument that needed to be selected and then be linked to the mentioned LabVIEW programme. Moreover, it was required that it would be possible to connect up to 7 additional thermocouples to be able to measure several temperatures at different positions of the furnace at the same time. Missing parts such as cables and adapter had to be chosen and connected.

3.3 The high pressure gas supply system

Figure 13 shows the layout of the high pressure gas supply system and the tube furnace.

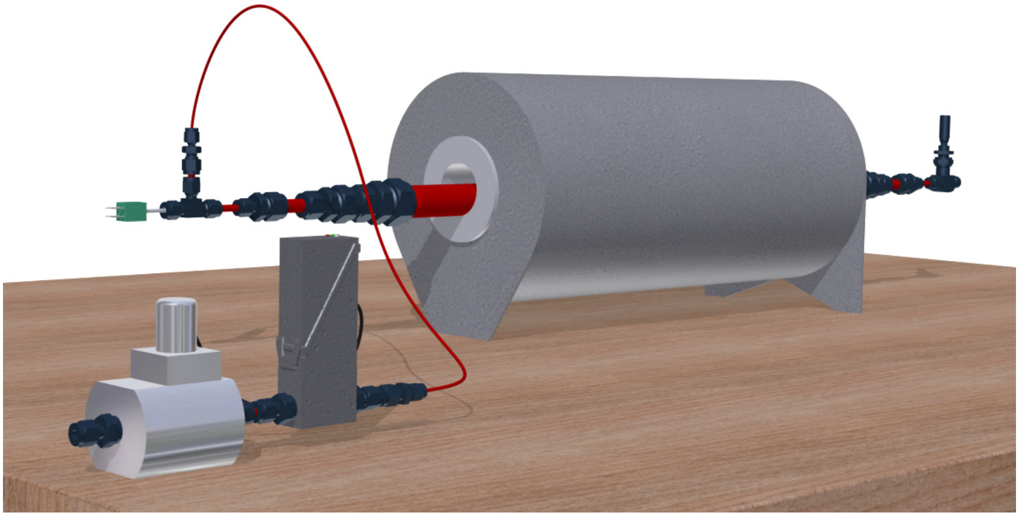

Figure 13. Model of the high pressure furnace with the installed high pressure gas supply system.

A simplified wiring diagram that consists of all relevant pneumatic components is shown in Figure 14. The pressure supply is first connected to a manual pressure reducer. This pressure reducer is used to roughly reduce the pressure coming from a gas cylinder whose pressure is 200 bar.

To adjust the pressure more precisely up to 100 bar a digital pressure controller in combination with a digital pressure meter is connected after the manual pressure reducer. Then the high pressure reaction cell where the samples are going to be put inside follows. The heat coming from the furnace is represented with a heat flow $\dot{Q}$ in the wiring diagram. The nickel-base alloy Hastelloy X-750 was chosen in former studies of the project [16] because of its oxidation resistance and strength at high temperature.

The leak valve is connected to the high pressure cell. It is used for a manual regulation of the volume flow of the process gas. The process gas flows then in ambient atmosphere.

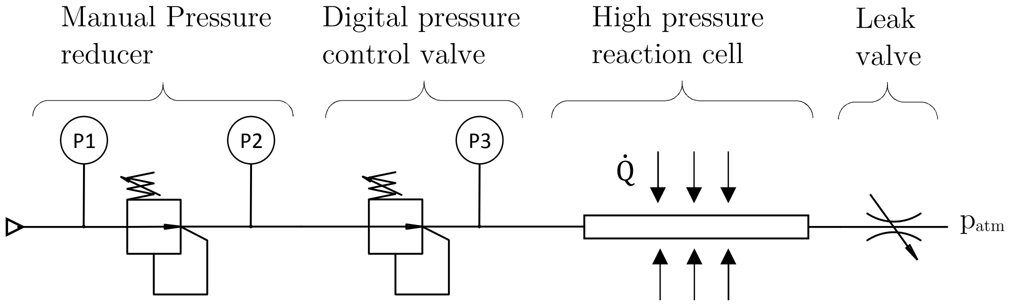

Figure 14. Wiring diagram of the high pressure gas supply system.

Swagelok tube fittings

The connections between the components are done using Swagelok fittings. The process which occurs during tightening the nut of a straight Swagelok standard fitting that connects two metal tubes with each other is explained below.

One side of a female Swagelok connector consists of a nut, two ferrules and a body part, as shown in Figure 15 a). After inserting the tube to be connected into the intended hole of the body part the nut needs to be tightened according to Swagelok's installer guide [17]. While tightening the nut (Pos. 1) the back ferrule (Pos. 2) and the front ferrule (Pos. 3) get strongly stressed in axial direction. Due to the wedge shaped chamber of the Swagelok body (Pos. 4) the ferrules are forced to move in radial direction where they come into contact with the tube. After the nut is fully tightened the two ferrules can no longer be removed because of the strong deformation.

A connection between two tubes by means of a straight Swagelok fitting is shown in a half-sectional view in Figure 15 b). This connection prevents the tubing from leakage up to several hundred bars depending on the diameter and the wall thickness [17].

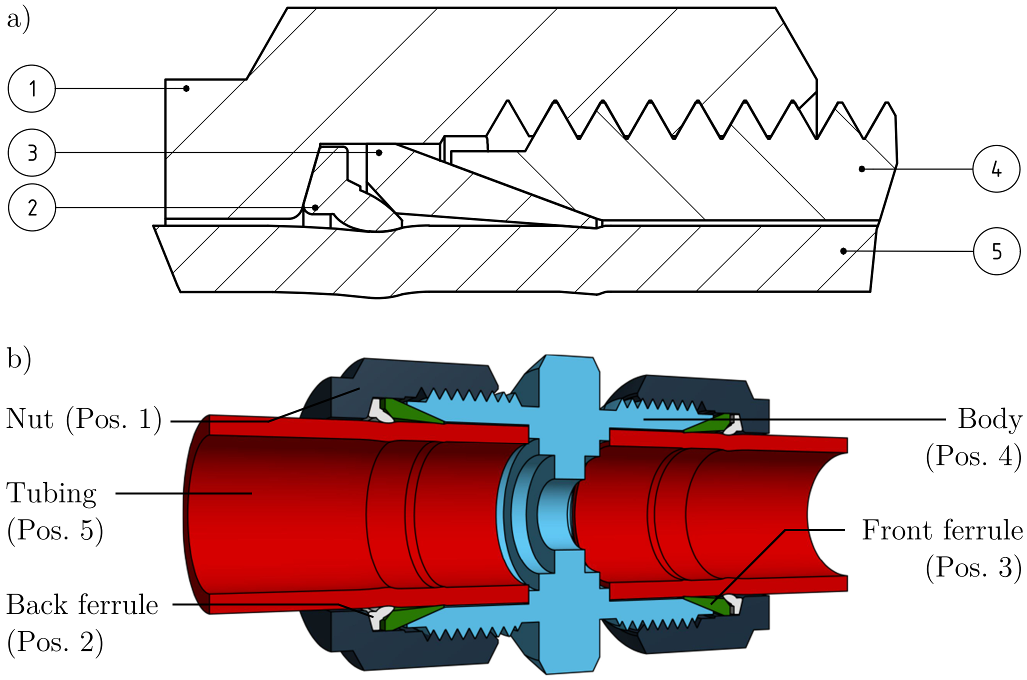

Figure 15. Principle of Swagelok fittings. a) Detail view of the inner parts. b) half-sectional view of a straight Swagelok fitting that fits two tubes of the same diameter.

For creating proper connections Swagelok Company recommends only the use of Swagelok tubing material. However, there might be special applications where there is no suitable tube provided by Swagelok, for example at very high operating temperatures. In this case Swagelok Company suggests the following properties for the tube:

- Hardness of tubing material must be maximal 90 HRB or 200 HV
- Tubing material has to be suitable for bending or flaring
- Outer diameter must be within the tolerance of ±0.076 mm

Due to the different resistance coming from the tube during installation depending on the tube dimensions Swagelok Company also limits the wall thickness. For a tube diameter of 25 mm, for instance, Swagelok Company guarantees sealing up to 260 bar while the wall thickness must be between 2.2 mm and 3 mm.

Temperature gradient along the high pressure reaction cell

The furnace concept with the sealing of the high pressure cell using Swagelok fittings assumes that the temperature of the high pressure cell extremities does not exceed 200 °C [18]. In order to validate this requirement the temperature gradient along the Hastelloy tube ends was measured.

The tube projects on each side by 120 mm when it is put inside the furnace. At this length the tube has to be connected for transferring the gas to the neighbouring parts.

Before measurements were taken the tube was heated up with a gradient of 160 °C per hour to a maximum temperature of 888 °C, where it stayed for one hour. The environmental temperature was 23 °C. Measurements were done using a type K thermocouple by TES model 1303 Thermometer by contacting the outer tube surface. The accuracy of the measuring device was about ±2 °C in the measured range. The measuring points start at the respective tube end which is referred to zero. So the bigger the distance from the end face the closer the measuring points are to the furnace.

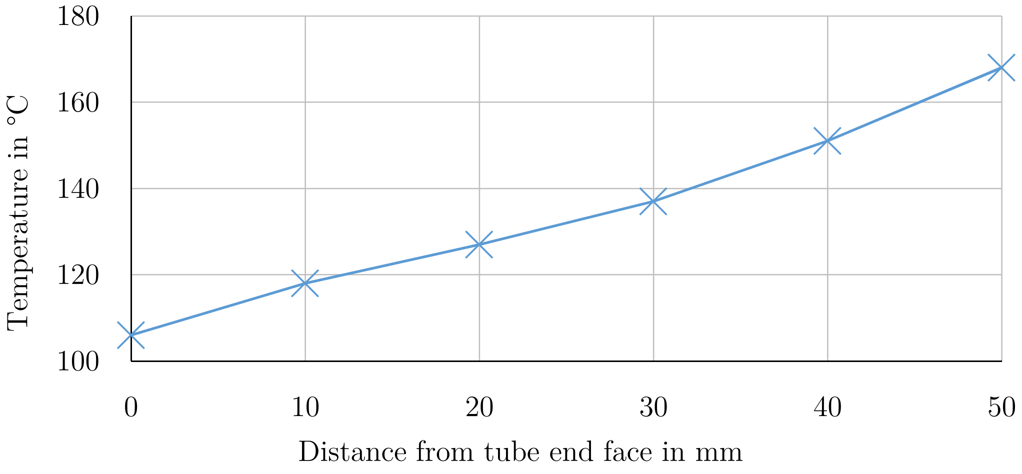

Figure 16. Temperature of the Hastelloy tube as a function of the distance to the tube end.

The graph in Figure 16 shows the temperature profile measured from both tube ends using an interval of 10 mm distance between the measuring points. It can be seen that there is an approximatively linear temperature increase for the first 50 mm from the tube end face. This length is enough to connect a conventional Swagelok tube fitting. It can be seen that the maximum temperature measured at the first 50 mm of the tube is about 170 °C, which is well below the limit of 200 °C that should not be exceeded.

It can be assumed that there will be roughly the same temperature at the connected Swagelok fitting (Pos. 2). For temperatures up to 537 °C Swagelok Company provides reducing factors [18] that have to be multiplied with the specified working pressures [17] of the respective part RT. Taking the present temperature of 200 °C this factor is 0.96. This factor reduces the applicable pressure only very slightly so there is almost no impact on the connection due to the temperature. That means that provided standard Swagelok fittings made out of stainless steel (SS 316) can be used.

Design of the high pressure gas supply system

For installing the pressure cell it is important that the Hastelloy tube fits together with the Swagelok fittings through the tube of the furnace so that it can be installed pre-assembled. All straight fittings from Swagelok provided for a diameter of 30 mm have an outer diameter of 57.7 mm at their biggest point so are too large to fit. In order to fit the pressure cell with fitting into the tube of the furnace the design of the Hastelloy tube had to be changed.

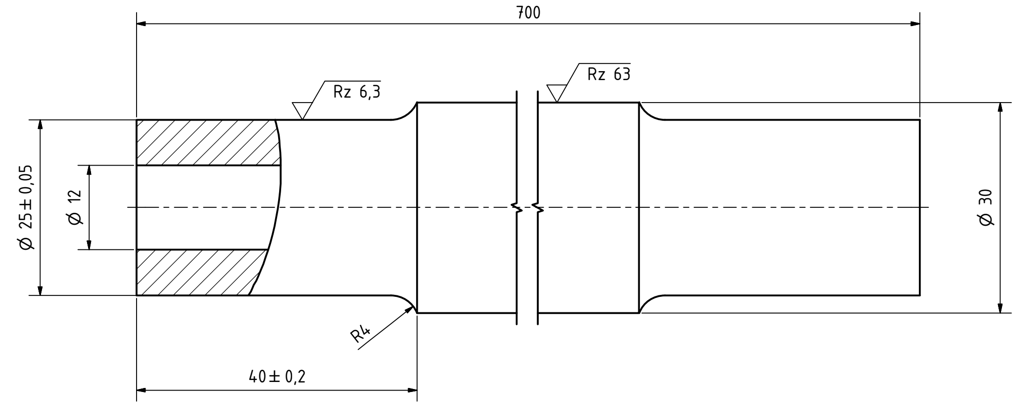

Figure 17. Design of the Hastelloy tube.

One possible solution was to turn the ends of the existing tube to a smaller diameter which allows the use of smaller fittings. In that case a tube diameter of 25 mm was chosen. The maximum diameter of the Swagelok fitting SS-25-M0-6-18 is 40.4 mm, which allows sliding the fully assembled high pressure cell into the furnace. The design for this solution is shown in Figure 17. To avoid getting a notch effect at the shoulder the tube has a 4 mm radius. For generating a proper seal the surface roughness was chosen to Rz 6.3.

Another solution would have been to drill an internal thread on both tube ends in combination with using a different type of Swagelok fitting. Such a fitting has a male thread on one side and a normal tube fitting on the other one. A suitable fitting would have been SS-15M0-1-8RP. It has a ½ inch outer thread, so the inner diameter of the tube ends would have had to be changed to the same thread size. But this thread has a maximum diameter of about 21 mm which means that the wall thickness would become only 4.5 mm at this connection range, whereby the solution shown in Figure 17 has a wall thickness of 6.5 mm. This would cause higher stresses to be induced at simultaneously same load.

On account of this, the first described design was chosen even though the wall thickness is not in the recommended range for Swagelok fittings.

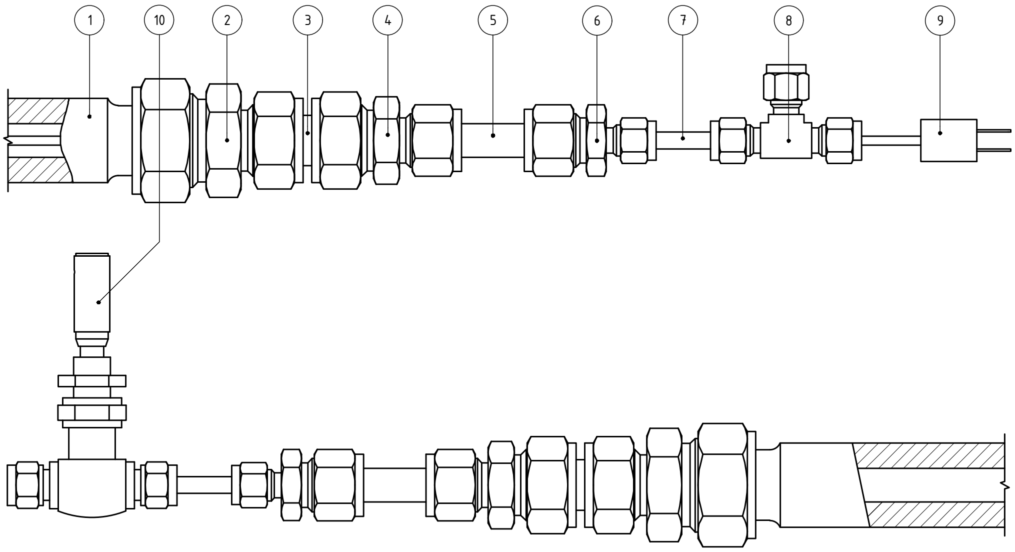

Figure 18. Tubing of the high pressure reaction cell.

Figure 18 shows all parts straight connected with the high pressure reaction cell. The leak valve and the pressure controller need to have a much smaller diameter for the connection. Therefore, it was necessary to reduce the tubing diameter. Since Swagelok doesn't provide a direct adapter from 25 mm to 6 mm many fittings were used.

As it can be seen the reaction cell consists of three connections. Respectively, one for gas inlet and outlet and another one for connecting the thermocouple. The rod of the thermocouple is inserted to the middle of the high pressure reaction cell where it is inserted into the sample holder.

Table 3. Parts list of the high pressure gas supply system.

Position	*Quantity*	*Part description*
1	1	Hastelloy X-750 tube
2	2	Swagelok fitting 25 mm to 18 mm
3	2	Swagelok Port Connector 18 mm
4	2	Swagelok fitting 18 mm to 12 mm
5	2	Tube Ø 12×40 mm
6	2	Swagelok fitting 12 mm to 6 mm
7	2	Tube Ø 6×30 mm
8	1	Swagelok Tee 6 mm
9	1	Thermocouple plus sealing
10	1	Leak valve
11	4	Swagelok Port Connector 6 mm
12	4	Swagelok fitting 6 mm to 1/8 inch
13	2	1/8 inch tube, 1 m length
14	1	Pressure meter/controller, P-522C-M40A-AGD-33V
15	1	Control valve, F-033C-LIU-33V

The parts list for the pressure gas supply system is shown in Table 3. For placing and replacing the wires in the sample holder it is necessary to open the high pressure reaction cell in order to loosen the connection between port connector (Pos. 3) and Swagelok fitting (Pos. 2). This connection was chosen because the port connector has a machined ferrule end so that it can resist more exchanging cycles than normal tube ends.

While losing and tightening the nut it is important that all the other connections stay properly closed to prevent unexpected leakage during the operating state. Thus, the nut that has to be used for the exchange is marked with red crosses on the plain sides so as not to mix it up with the others. After loosening this nut Pos. 2 to 9 can be pulled out of the pressure cell and the samples can be exchanged.

At the inlet fitting tee (Pos. 8) the pressure control valve and a pressure meter are connected over a flexible 1/8 inch (Pos. 13) tube, as shown in Figure 19. In order to fit the tube to the surrounding components another Swagelok fitting (Pos. 12) in combination with a port connector (Pos. 11) is assembled on both tube ends.

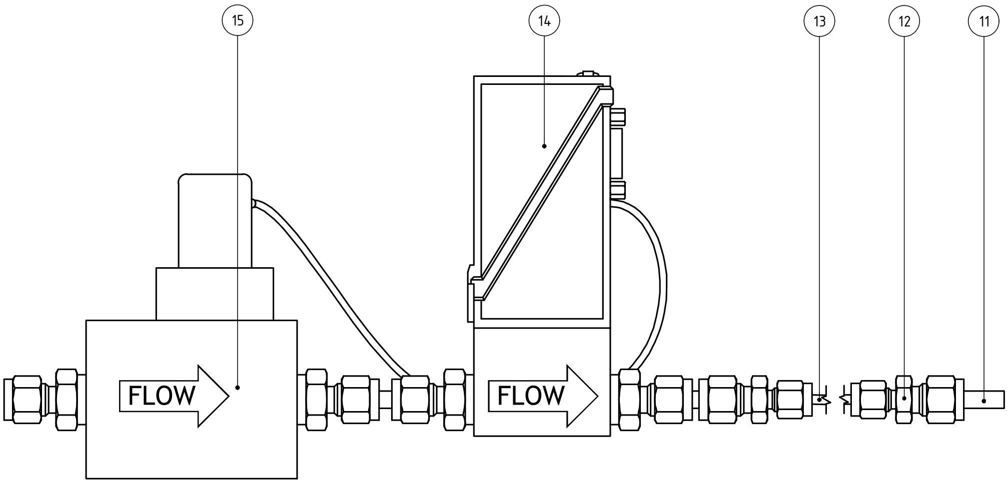

Figure 19. Tubings from the high pressure cell to the pressure control valve.

From the pressure valve another flexible tube (Pos. 13) with the fittings (Pos. 12) and port connector (Pos. 11) is installed to get to the manual pressure reducer which is directly connected to a gas cylinder.

3.4 Safety investigation of the high pressure cell

The weakest connection of the high pressure cell is the connection between the Hastelloy X-750 tube (Pos. 1) and the Swagelok fitting (Pos. 2), because the wall thickness is 6.5 mm, 3.5 mm higher than recommended from Swagelok Company.

During the OP processing a maximum total pressure of 100 bar will be reached at a temperature, in the centre of the high pressure cell, of 900 °C. As shown in Figure 16, the temperature at the tube extremities does not exceed 200 °C.

Since a temperature of 200 °C has little effect on the maximum applicable pressure coming compared to RT, the test was performed at RT. In order to guarantee as much safety as possible the high pressure cell was loaded with nearly the maximum pressure that Swagelok approved for 3 mm thick tubes [17]. So a test pressure of 250 bar at RT was chosen.

Strength calculation

Before the high pressure cell was tested the stress of the material was investigated to see whether the tube and the connection would theoretically withstand the load of 250 bar.

Table 4. Material properties of the Hastelloy tube used [19].

elongation at break in %	*tensile strength at break in MPa*	*0,2 % yield strength in MPa*
23,6	1325	975

Due to its high elongation at the breaking point [19], shown in Table 4, the Hastelloy tube can be assumed to a ductile material. This means that the von Mises equation for hollow cylinders [20] below can be used to calculate the maximum stress.

$$\sigma_v = p_i \cdot \frac{\sqrt{3} \cdot u^2}{u^2 - 1} \tag{3.1}$$

Where

u	is the diameter ratio
p_i	is the inner pressure of the tube

With the diameter ratio:

$$u = \frac{d_o}{d_i} \tag{3.2}$$

Where

d_o	is the outer tube diameter
d_i	is the inner tube diameter

For the present tube, with an outer diameter of 25 mm and an inner diameter of 12 mm, the maximum von Mises stress at 250 bar is 56.3 MPa.

Comparing the load to the maximal supportable stress, the safety factors against plasticity, S_f, (see Equation 3.3) and break, S_b, (see Equation 3.4) can be calculated.

$$S_f = \frac{\sigma_f}{\sigma_v} \qquad 3.3$$

Where

σ_f is the yield point

$$S_b = \frac{\sigma_b}{\sigma_v} \qquad 3.4$$

Where

σ_f is the tensile strength at break

Using the values from Table 4, the safety factors are S_f=17.3 and S_b=23.5. According to this calculation the tube is far away from any kind of plastic deformation.

To verify the connection between the Hastelloy tube and the port connector the axial force coming from the pressure was also calculated. In a simplified model the cross-sectional area of the tube can be used to calculate the force:

$$F = p \cdot A \qquad 3.5$$

Where

p is the pressure
A is the projected face of the outer tube diameter

For a diameter of 25 mm and a pressure of 250 bar the axial force is 12 272 N. This value is compared below to implemented test results that have been performed by Swagelok Company.

According to a tensile test that was done by Swagelok Company the connection withstands a force of 45 000 N. A Swagelok connection was tested using a fitting to connect two tubes made out of stainless steel 316 with an outer diameter of 25 mm and a wall thickness of 3 mm. The tubes were then put under tension in the axial direction with an extension of 9.5 mm per minute until either the tube pulled out of the fitting or the tube fractured [21]. Comparing these results directly to those of the above calculation is not valid because there are differences in material and wall thickness. However, it shows that a connection according to Swagelok recommendations would easily withstand the load.

High Pressure test

A high pressure test was performed in order to verify that the high pressure tube and all fittings can be safely pressurised. The pressure test was implemented at a pressure test facility at CERN. Figure 20 shows the high pressure cell during the pressure test at the maximum load of 250 bar.

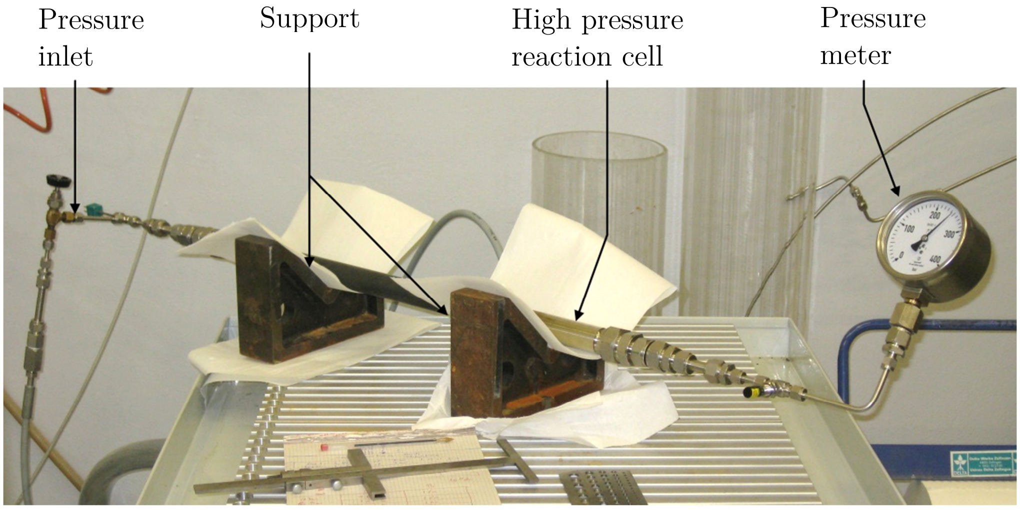

Figure 20. Hydraulic pressure test of the high pressure reaction cell at the maximum pressure load of 250 bar at RT.

The inlet of the high pressure gas supply system is connected to a hydraulic water system while it rests on a free support that can theoretically allow deformation in all directions. At the outlet a pressure meter was connected to output the current pressure inside the system. The pressure load was increased to its maximum in 50 bar steps. After every step the pressure was held for a brief moment to measure the axial length between the Swagelok fittings (Pos. 2 and Pos.6) on both sides using a Vernier calliper.

Once the maximum pressure of 250 bar was achieved the load was held for one hour to see whether there is any change in pressure or length. As shown in Table 5 there was no significant change in dimension during the pressure test [22]. The pressure drop after 1 h was zero.

After the performed test the water was completely removed from all tubing, to not affect the material, using compressed air.

Table 5. Measurement results [22] of the tube end lengths while increasing the pressure.

Applied pressure in bar	Length (inlet) in mm	Length (outlet) in mm
0	161.0	160.0
60	161.5	160.0
100	161.5	160.0
150	161.5	160.5
200	161.5	160.5
250	161.5	160.5
250 (after 1 h)	161.5	160.5

3.5 Pressure control and temperature recording

3.5.1 Hardware components

The pressure controller and control valve

The used pressure controller from Bronkhorst, shown in Figure 21, has a proportional–integral-derivative (PID) controller and pressure meter inside. It is directly connected, using Swagelok fittings, to a pressure control valve that represents the actuator in the closed-loop pressure control. Therefore, it is also electrically connected to the pressure controller.

Figure 21. Electronic forward pressure controller.

The pressure meter uses the piezo resistive effect to measure absolute pressures, as explained in chapter 2, from 1 to 100 bar [16], with a pressure accuracy of ±0.5%. The measured pressure is read out using the RS-232 interface, which is also used to configure the PID controller.

The control valve works with the so called ‘Vary-P principle’ from Bronkhorst. That means that it consists of two valves, where one is electromagnetic and the other one is a pressure compensation valve. This enables precise pressure control at very high pressure drops.

The pressure controller is certified with International Protection (IP) 40. So there is protection against particles down to 1 mm size, but none against water. In accordance with this the control valve can only operate in dry environments.

The temperature sensor

The temperature of the Bi-2212 samples is measured by means of two type S thermocouples by Therma Thermofühler GmbH, because of the good temperature accuracy at high temperatures (see chapter 2). For the temperature range of the HT the temperature error is ± 1 °C. However, this is not the final accuracy of the temperature measured because the uncertainties of the measuring device also have to be taken into account. This is described in the next paragraph.

The data acquisition instrument

Based on the requirements mentioned in 3.2 an embedded control and acquisition system from National Instruments (NI), called compact reconfigurable input output (cRIO) 9030, was selected in agreement with the LabVIEW team at CERN. Moreover, to provide a plug for the thermocouples, the thermocouple module NI 9214, which can be added into the cRIO chassis, was chosen.

This hardware was selected because of its rugged hardware design and high accuracy of measurement. Furthermore, for future upgrades, the cRIO system provides three more plugs for the connection of other modules. One extension could be, for instance, a temperature control upgrade, that would replace the Honeywell digital controller to improve the temperature precision during the HT. Another advantage is that the cRIO controller can be connected to the network so that measurements could be monitored via the internet.

The thermocouple module provides a reference thermometer and 16 channels that can also be used for other thermocouple types. The highest achievable accuracy of the thermocouple module in the temperature range from 300 °C to 900 °C for S-type thermocouples is ±0.6 °C [23]. This accuracy is achieved only at a reference temperature from 20 °C to 30 °C and using the high resolution mode in LabVIEW. Taking also the maximum error of the thermocouple itself into account the measured temperature accuracy is within a tolerance of ±1.6 °C.

The electrical wiring

To facilitate the electrical wiring the cRIO chassis is placed in a switchboard on a DIN rail (EN 50022 – 35×7.5), as shown in Figure 22.

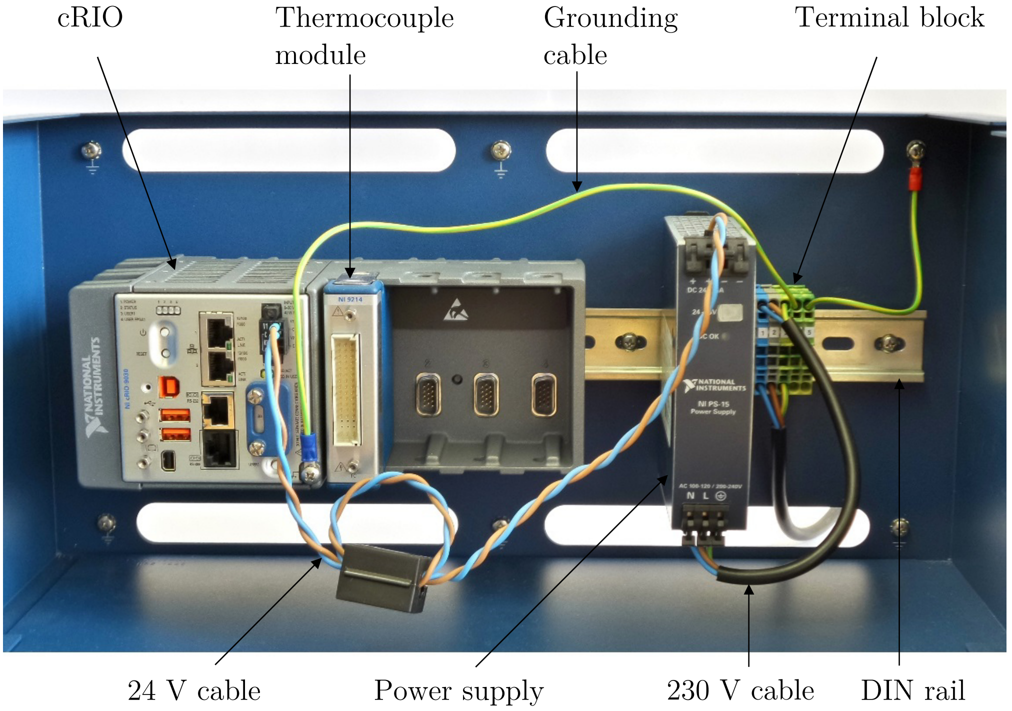

Figure 22. Switchboard with cRIO, thermocouple module and power supply unit.

The system is connected to a one phase 230 V supply. The incoming three wires, phase, neutral and ground, are first connected to a terminal block (pin 1-3). The terminal block is used to distribute the incoming grounding conductor (pin 3-5) to the cRIO chassis, the switchboard and the power supply.

The thermocouple, which is used for the temperature recording, is connected to the thermocouple module. Its wires are connected via a bolted fastening to channel one of the terminal block.

In order to connect the pressure controller with the cRIO controller an adapter was soldered according to the hook-up diagram [24] in Figure 23 a). The D-Sub plug is connected with the RS-232 interface of the cRIO controller. To provide the required operating voltage for the pressure controller, a 19.5 V notebook power supply is connected to the plug shown on the bottom of Figure 23 b).

For the commissioning of the OP furnace the cRIO controller was connected via a USB cable to the host computer on which LabVIEW and all drivers for the cRIO were installed according to [25].

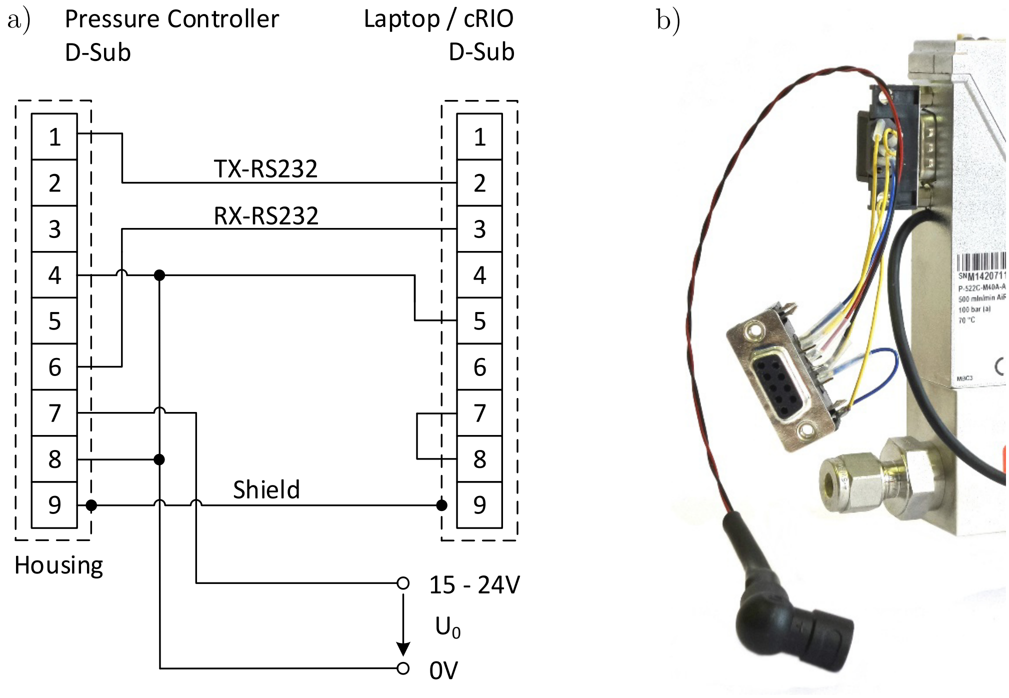

Figure 23. a) Hook-up diagram for the RS-232 [24]. b) Photograph of the soldered adapter connected to the pressure controller.

3.5.2 Hardware configuration and LabVIEW program

Configuration of the closed loop control parameter

Figure 24 shows the block diagram [26] of the used pressure controller. The control parameters (K_{speed}, K_P, T_I, T_D) of the PID pressure controller have a default value. When these need to be changed the pressure controller has to be connected via serial port, using the soldered adapter (see Figure 22), to a PC or laptop on which the programs ‘FlowDDE’ and ‘FlowPlot’ by Bronkhorst are installed. For this connection it is recommended to use the physical serial port (COM port) of the PC because many tested USB-to-serial adapters weren’t stable. Used were FlowDDE version 4.69 and FlowPlot version 3.34.

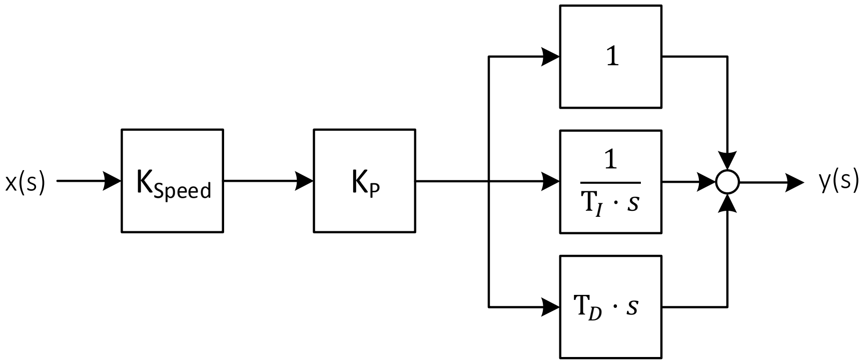

Figure 24. Block diagram of the PID pressure controller [26].

When the pressure controller is connected it has to be turned on and FlowDDE has to be opened. Then the communication to the pressure controller needs to be opened according to [27]. After opening the communication FlowPlot can be started. The parameters for the pressure controller can be found under ‘instrument settings’ on the main window of FlowPlot. All conducted changes will be permanently saved. Before disconnecting the pressure controller the opened communication in FlowDDE should be closed.

User interface for temperature recording and pressure regulation

The program for the operating high pressure furnace is based on the Bronkhorst FLOW-BUS Instrument Control Application that is part of the certified LabVIEW plug and play driver downloaded from Bronkhorst [28].

With this programme it is possible to enable the communication to the pressure controller and to control manually set constant pressure values. It also reads out the current pressure of the pressure meter and the position of the control valve.

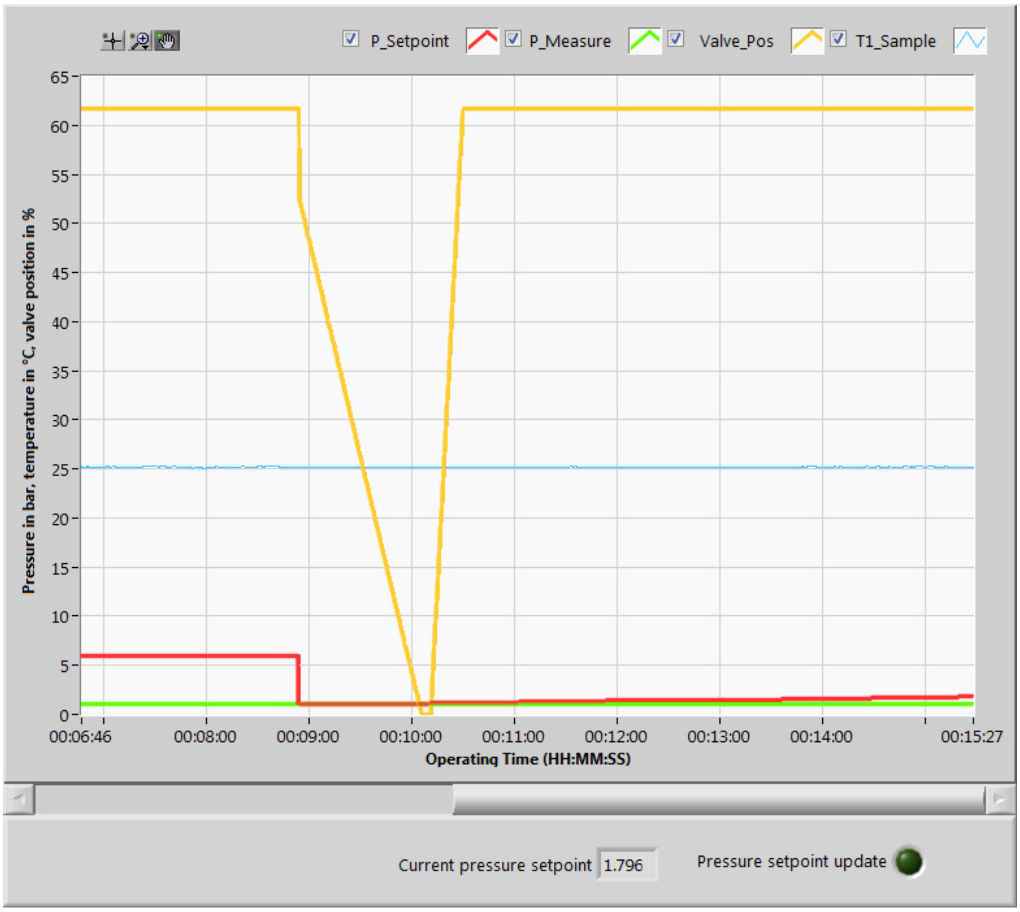

Current pressure setpoint 1.796

Figure 25. Information window of the running programme for the OP furnace, where all important measurements are plotted in one graph.

This LabVIEW programme had been modified in order to add an automatic pressure setpoint control that allows the programming of predefined pressure curves for HT of the Bi-2212 wires to be performed. Also, the temperature acquisition for the thermocouple was added. For that a new NI project called ‘High Pressure furnace’ was created. The project needs to be opened from the PC. It is automatically uploaded on the cRIO when it is started.

The surface of this program is divided into two main windows. The first window contains a graph, shown in Figure 25, which plots the acquired data such as nominal and current pressure, temperature and valve position.

All controls and settings are done on the second window, shown in Figures 26 and 27, where the different control operations are classified in different tabs. Explained below are the ‘Setting’ and the ‘Automatic Pressure Control’ tab.

When the HT of the OP furnace is to be performed under high pressure the connection to the pressure controller must be established. This is done by clicking connect in the ‘settings’ tab, whereby the parameters need to be set according to Figure 26. To validate the connection to the pressure controller the wink button can be clicked. When the connection is working the LED’s of the pressure meter start to blink. Below the communication, a directory where the data shall be saved has to be defined. The data can either be saved on a USB stick or on the hard drive of the cRIO.

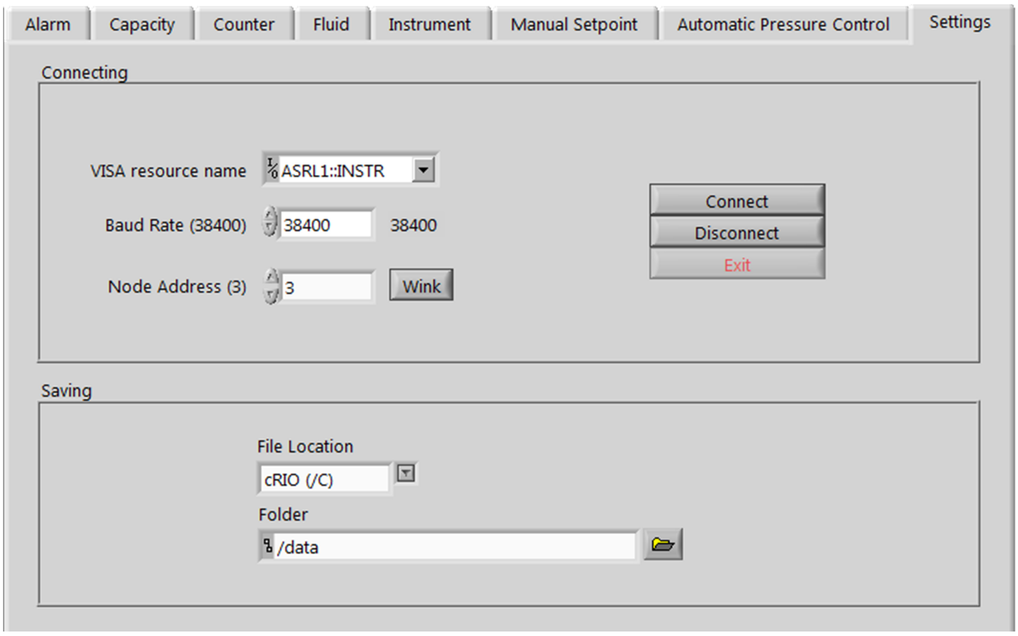

Connecting

VISA resource name: ASRL1::INSTR

Baud Rate (38400): 38400 38400

Node Address (3): 3

Saving

File Location: cRIO (/C)

Folder: /data

Figure 26. Settings of the LabVIEW program.

In the ‘Automatic Setpoint Control’ tab (see Figure 27) the pressure that shall appear over time during the HT is defined in the ‘Setpoint Control’ table. In this table the pressure ramp rates and the durations of delay have to be added. It is required to use the same notation as explained for the HT, meaning that the odd numbers are used for pressure ramp rates and the even numbers for pressure plateaus. When clicking the update button the defined curve appears on the graph below the table.

The graph shows the exact curve that has been defined in red and a curve that is interpolated between the relevant points of the exact curve in green. The pressure setpoint is going to be updated when the value of the green curve has changed. For this the precision of the pressure setpoint can be defined by changing the control ‘number of digits after decimal point’. The LED on the bottom right hand side in Figure 25 flashes when a new pressure setpoint is sent to the pressure controller.

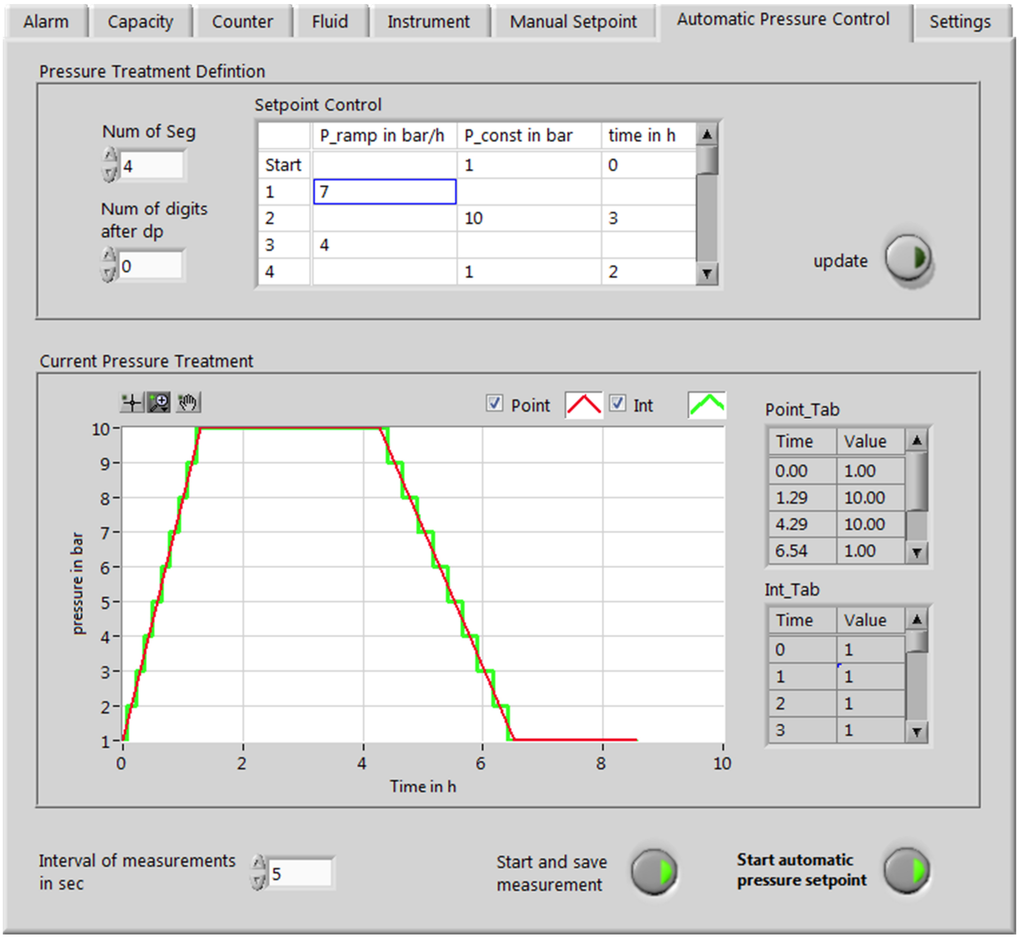

Pressure Treatment Defintion

Num of Seg: 4

Num of digits after dp: 0

Setpoint Control

	P_ramp in bar/h	P_const in bar	time in h
Start		1	0
1	7		
2		10	3
3	4		
4		1	2

Current Pressure Treatment

Point_Tab

Time	Value
0.00	1.00
1.29	10.00
4.29	10.00
6.54	1.00

Int_Tab

Time	Value
0	1
1	1
2	1
3	1

Interval of measurements in sec: 5

Figure 27. Automatic pressure control tab of the running program.

The measured data is saved in an excel sheet, with an interval chosen on the bottom of the ‘automatic pressure control’, to the previously mentioned file location when the ‘start and save’ switch is active. The LabVIEW program can be closed by clicking disconnect and the exit button in the settings.

4 Investigation of the Bi-2212 wire processing HT

4.1 The in situ XRD experiment at the ESRF

Five days of beamtime had been allocated to continue the study of the influence of the p_{O2} on the phase changes during the processing of Bi-2212 wires (experiment name MA2311). The long-term objective of this study is to determine the p_{O2} margins in which Bi-2212 melt processing is possible, and to measure the temperatures at which the different phase changes are occurring in dependence of p_{O2}. The temperature measurement accuracy is, therefore, of outmost importance for the present experiment.

An already existing set-up [29] was used at ESRF ID15B for combined *in situ* high energy X-ray diffraction investigations of Bi-2212 processing at variable process gas pressure and temperatures. The system consists of an X-ray transparent furnace that is placed around a high pressure cell. The high pressure cell is connected to a gas supply line and consists of a single crystal sapphire tube in which the sample is placed.

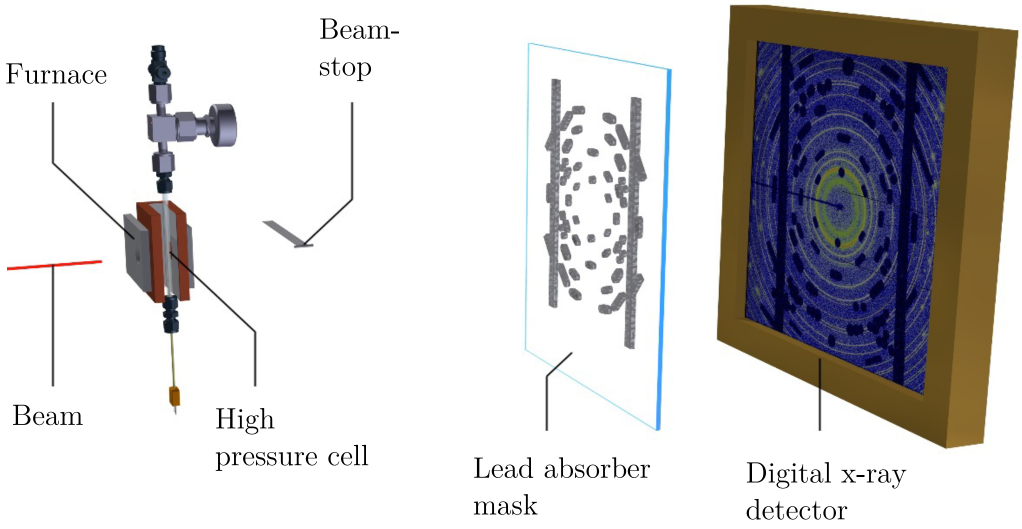

Figure 28. Simplified experimental setup at the high energy synchrotron beamline ID15B.

A sketch of the experimental setup that was used for the *in situ* synchrotron XRD experiments at variable temperature and pressure at the beamline

ID15B can be seen in Figure 28. The cross section of the 87.14 keV monochromic beam was 0.3×0.3 mm. The diffracted beam was acquired by the two dimensional detector (Perkin Elmer XRD1621 CN3-ES). This detector has 2048×2048 pixels and a pixel size of 200 µm.

In order to not acquire diffracted X-rays from the single crystal sapphire tube the sapphire diffraction spots are absorbed by means of a lead mask that is placed in front of the detector. The position of the lead absorbers on the mask needs to correspond with the diffraction pattern of the single crystal sapphire tube. The X-ray absorption in the plastic plate onto which the lead absorbers are mounted is negligible.

A photograph of the experiment installed at the ID15B beamline is shown together with the experiment team in Figure 29.

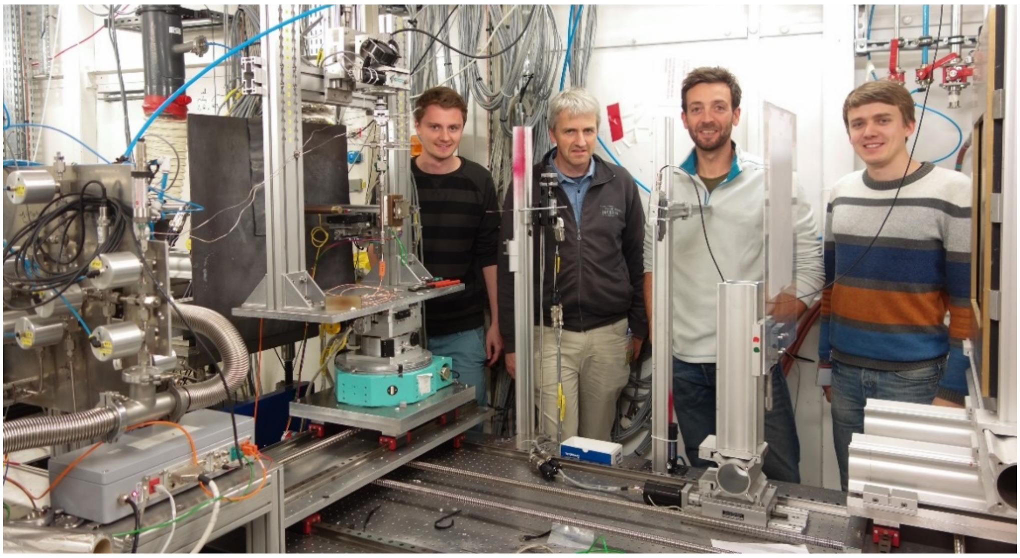

Figure 29: Installed setup of the experiment at ID15B with the experiment team.

The high pressure cell with an instrumented Bi-2212 wire is shown in Figure 30 a). The pressure line is connected to the cross fitting of the high pressure cell. The pressure regulation works as an on-off control. When the pressure inside the cell becomes too high due to temperature increase of the process gas, an electropneumatic controlled valve that is connected to the outlet of the cross fitting will open for a short moment until the pressure drops below a set minimum. The switching hysteresis can be set accurately up to about 0.2 bar. The p_{O2} inside the high pressure cell was varied by changing the total pressure of the process gas (air zero X50S from Airproducts with an oxygen content of 20.9±1%).

The temperature reading during the HT was done by means of a type S thermocouple that was spot welded onto the Bi-2212 sample. This temperature measurement was also used to control the furnace temperature.

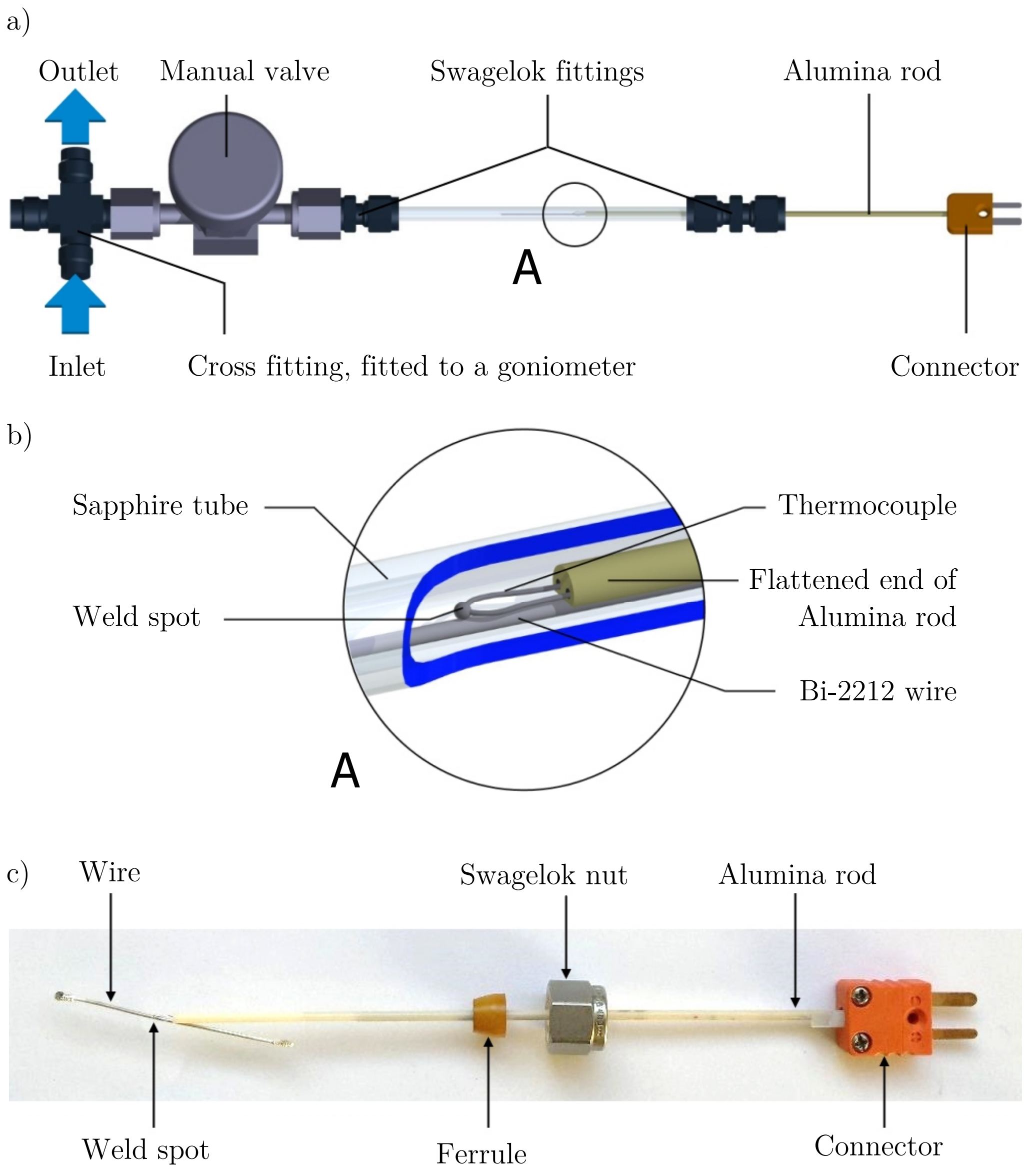

Figure 30. a) High pressure cell with instrumented Bi-2212 wire. b) Detailed view of the weld spot. c) Photograph of the Bi-2212 wire outside the high pressure cell.

The free connection of the cross shown in Figure 30 a) is installed to a goniometer which was used to align the high pressure cell perpendicular to the beam. During one acquisition the high pressure cell rotates ±40 degrees in order to homogenise powder diffraction rings [30]. The sample alignment was verified by means of a surveyor's level by which it was guaranteed that the beam hits the sample in the whole rotating range.

After the sample was aligned the furnace moved in the y-direction shown in Figure 31 until the bore in the furnace was centred to the beam. During the experiment the XRD pattern and all the important information like the pressure inside the sapphire tube and furnace and sample temperature were recorded. Temperature measurements were always performed at the beginning of a diffraction measurement, where the detector used an exposure time of 15 seconds.

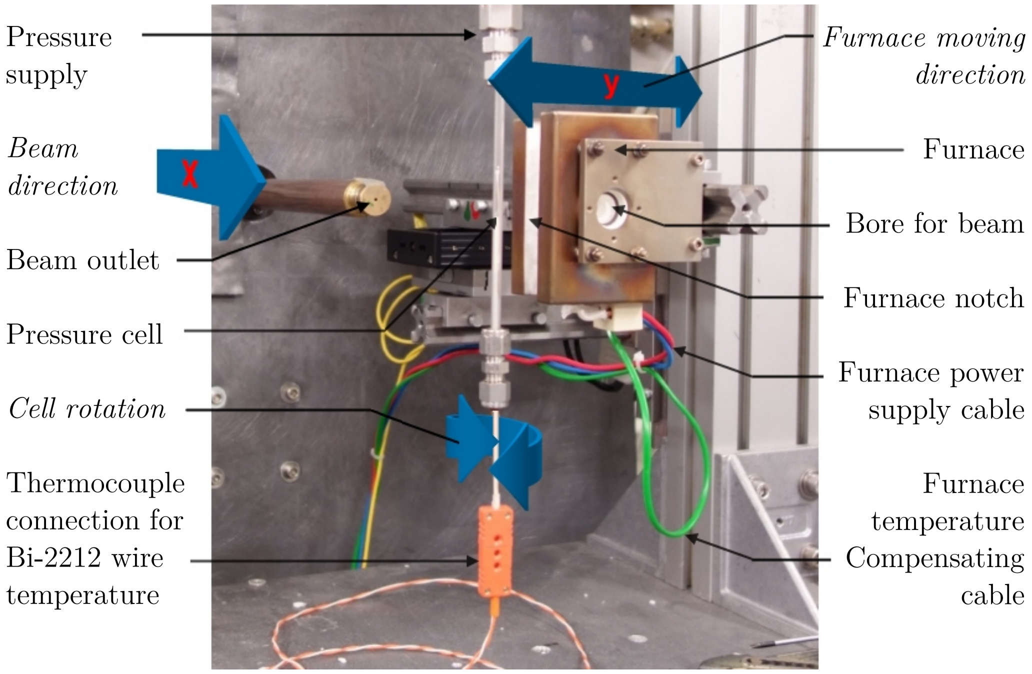

Figure 31. High pressure cell connected to the gas line at beamline ID15B at the ESRF.

Assembly of the X-ray transparent high pressure cells

Bi-2212 samples used for the diffraction experiments were about 5 cm long and prepared with closed ends by National High Magnetic Field Laboratory (NHMFL) Applied Superconductivity Center (ASC). The wires of the thermocouple were inserted in a double bored Alumina rod with an outer diameter of 2.2 mm such that they were unable to touch each other. The about 15 cm long alumina rod is machined at the end as shown in Figure 30 b). This small cut-out is necessary to fit the otherwise to wide alumina rod plus wire inside the sapphire tube.

To fix the thermocouple in its position and to prevent an uncontrolled leakage the wires of the thermocouple were glued with the alumina rod by using a two-component adhesive. The Bi-2212 sample in Figure 30 c) is inserted into a monocrystalline sapphire tube that can resist up to 200 bar at 1000 °C [29].

The assembling steps of the high pressure cell are listed below:

1) Machine to length and machine cut-out of alumina rod
2) Cut the Bi-2212 wire to the required size
3) Insert the wires of the S-type thermocouple into the bores of the alumina rod
4) Spot-weld the wire to the junction of the thermocouple
5) Glue the thermocouple to the alumina rod
6) Put Swagelok nut and ferrule onto the alumina rod
7) Wire the pins of the thermocouple to the connector
8) Connect the nut to the Swagelok fitting, sapphire tube and the valve

Performed *in situ* HTs

The *in situ* HT cycles that were performed during the beamtime (MA2311) are shown in Figure 32. One diffraction image was acquired every 5 minutes, whereby the total HT duration was lasting up to 20 hours, which corresponds to 240 diffraction images.

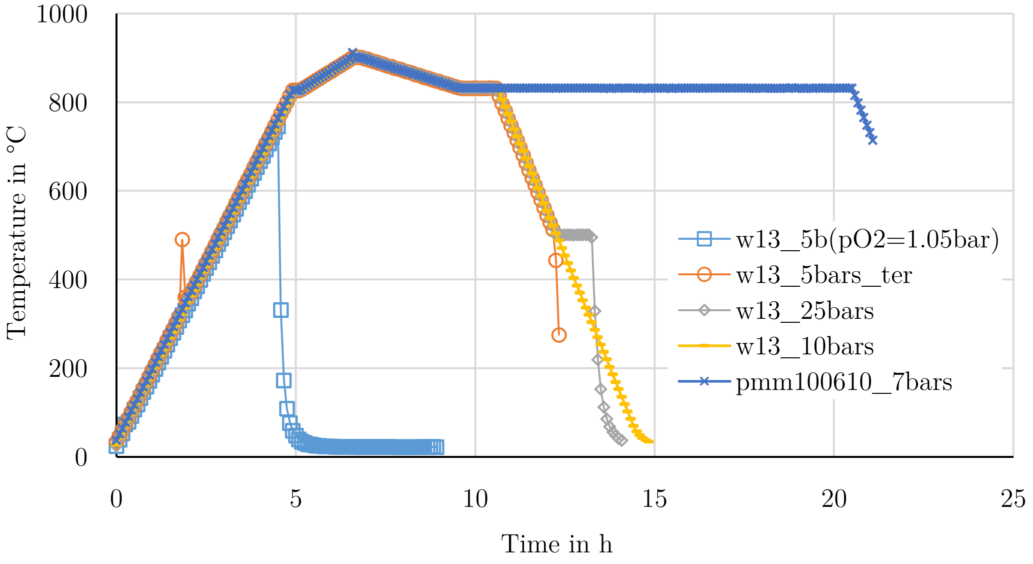

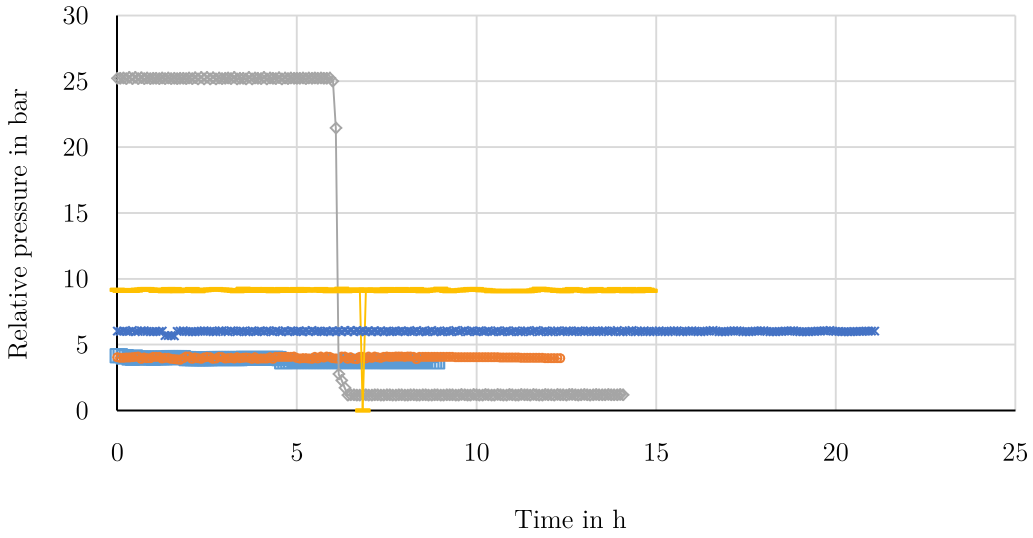

Figure 32. In situ HT and pressure cycles during beamtime MA2311.

4.2 XRD data analysis

In order to verify the thermocouple sample temperature measurements during the *in situ* HTs, the Ag lattice constants had to be determined from the acquired diffractograms as a function of this temperature. For that, the beam wavelength needed to be calibrated and the diffractograms had to be radially integrated. Moreover, a MATLAB script had to be developed which enables automatic Ag peak fitting.

For the experiments several preparations had to be done. One of them was the assembly of the sample to be investigated into the transparent high pressure cells. Furthermore, the setting up of the experiment and the sample alignment for every experiment needed to be done in cooperation with the team at the beamline.

4.2.1 Calibration of the beam wavelength

The calibration of the photon beam wavelength was done by means of the well-known lattice parameters of diffraction patterns of Cerium Dioxide (CeO_2) powder from the National Institute of Standards and Technology (NIST) [31], using the software FIT2D [32].

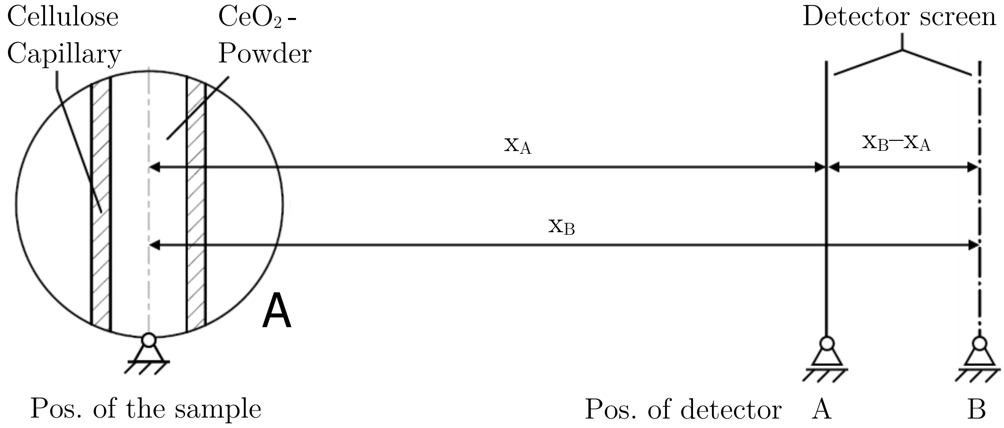

Figure 33. Set-up at ID15B for the calibration of the beam wavelength.

A schematic view of the set-up for the beam calibration is shown in Figure 33. Diffraction patterns were acquired with the two different sample-to-detector distances x_A and x_B, with $x_B–x_A=150$ mm. The exact beam wavelength was calculated using an iterative procedure (see Table 6).

In the present case an approximate wavelength of 0.14250 Å and a sample-to-detector distance of 1570 mm have been assumed as a starting value.

Table 6. Iterative steps for calibration of the beam wavelength.

Step *n*	λ *in Å*	x_A *in mm*	x_B *in mm*	$x_B - x_A$ *in mm*	*D* *in mm*
initial	-	~1570.000	~1420.000	-	-
1	0.14250	1570.083	1420.315	149.768	0.232
2	0.14228	1572.559	1422.574	149.985	0.015

With the data of the initial step and the assumed wavelength, FIT2D calculates the approximate powder-to-detector distance for the two detector positions. Comparing the difference of these positions with the known 150 mm detector shift makes it possible to see how precise the estimated wavelength is. The deviation between the difference (x_B–x_A) and the pre-set detector shift of 150 mm is referred to D.

When this deviation D is zero the wavelength is most precisely defined. In reality it is sufficient to do the iteration until the deviation is smaller than 0.1 mm. Using the deviation of the current step as an indicator for the wavelength of the next step shortens the iteration. The following equation corrects the previously used wavelength by a linearized term. The correction term is higher the higher the deviation is

$$\lambda_n = \lambda_{n-1} - \lambda_{n-1} \cdot \frac{D_{n-1}}{150\,mm} \tag{4.1}$$

Where

λ	is the wavelength
n	is the step number
D	is the deviation between x_B–x_A and 150 mm

After the second iteration step the deviation was 0.015 mm and thus the wavelength was calibrated to λ=0.14228 Å.

The beam energy can be calculated from the wavelength by following equation.

$$E = h \cdot \frac{c}{\lambda} \tag{4.2}$$

Where

h	is the Planck constant 6.62606957×10^{-34} m^2kg/s
c	is the speed of light 299 792 458 m/s
λ	is the wavelength

The photon wavelength of 0.14228 Å corresponds to an energy of 87.14 keV.

d-spacing error as a function of the sample-to-detector distance

The d-spacing error that is caused by an error of the sample-to-detector distance is calculated below. For this purpose the d-spacings of an *ex situ* sample 'w13_888 °C' have been calculated for different sample-to-detector distances.

First the radius of the diffracted ring was calculated for d-Ag(111)=2.3610 Å and d-Ag(220)=1.4457 Å at a sample-to-detector distance of x=1572.6 mm using Equation 2.2. With the same equation theta was calculated as a function of the sample-to-detector distance at a constant radius of the diffraction ring. For each theta the d-spacing was calculated with Bragg's law (see Equation 2.1).

Table 7 shows the influence of the sample-to-detector distance errors on the apparent d-spacing of the Ag(111) and Ag(220) peaks at RT.

Table 7. Influence of sample-to-detector distance errors on the apparent d-spacing of the Ag(111) and Ag (220) peaks at RT.

Sample-to-detector distance in mm	*d Ag(111) in Å*	*d Ag(220) in Å*
Measured value 1572.6	2.3610	1.4457
±1 (1571.6-1573.6)	2.3595-2.3625 (±0.064%)	1.4448-1.4466 (±0.062%)
±2 (1570.6-1574.6)	2.3580-2.3640 (±0.127%)	1.4439-1.4475 (±0.125%)

4.2.2 Radial integration of diffraction images

The radial integration was done by using the file series integration function from the FIT2D program. It allows the integration of all the files of one *in situ* experiment at once. The first and the last diffraction file need to be loaded as input.

In order to exclude the detector areas that were covered by lead masks from the radial integration, the mask shown in red was used. The regions shown in red are not taken into account for the integration. The already existing mask that was made to absorb the single sapphire diffraction spots was loaded with the command window of FIT2D.

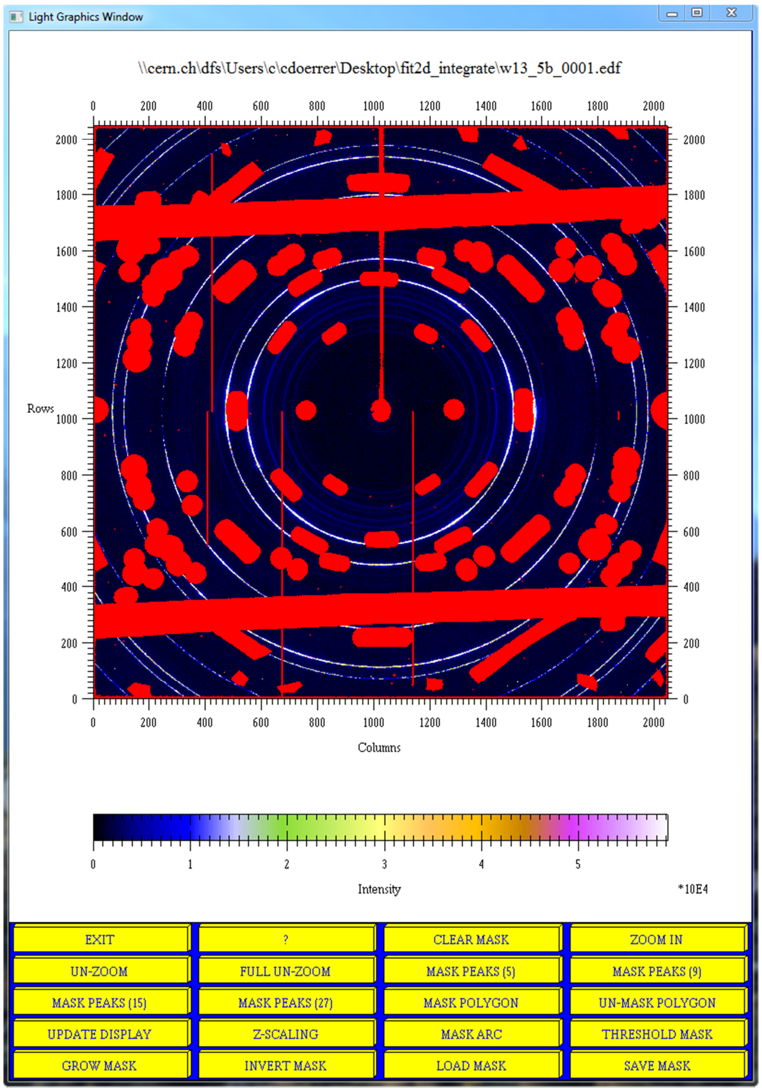

Figure 34. Diffraction image of a Bi-2212 wire with the overlaid mask showing in red the detector regions where lead blocks absorbed the diffraction spots of the sapphire single crystal high pressure cell. These areas have not been radially integrated.

The values that have been chosen for the experimental geometry are shown in Figure 35. The position of the beam centre has been determined by measuring the centre of the diffraction rings using FIT2D. The integrated intensity values have been saved as a function of

$$Q = \frac{2\cdot\pi}{d} \tag{4.3}$$

where

d is the distance of two parallel lattice planes.

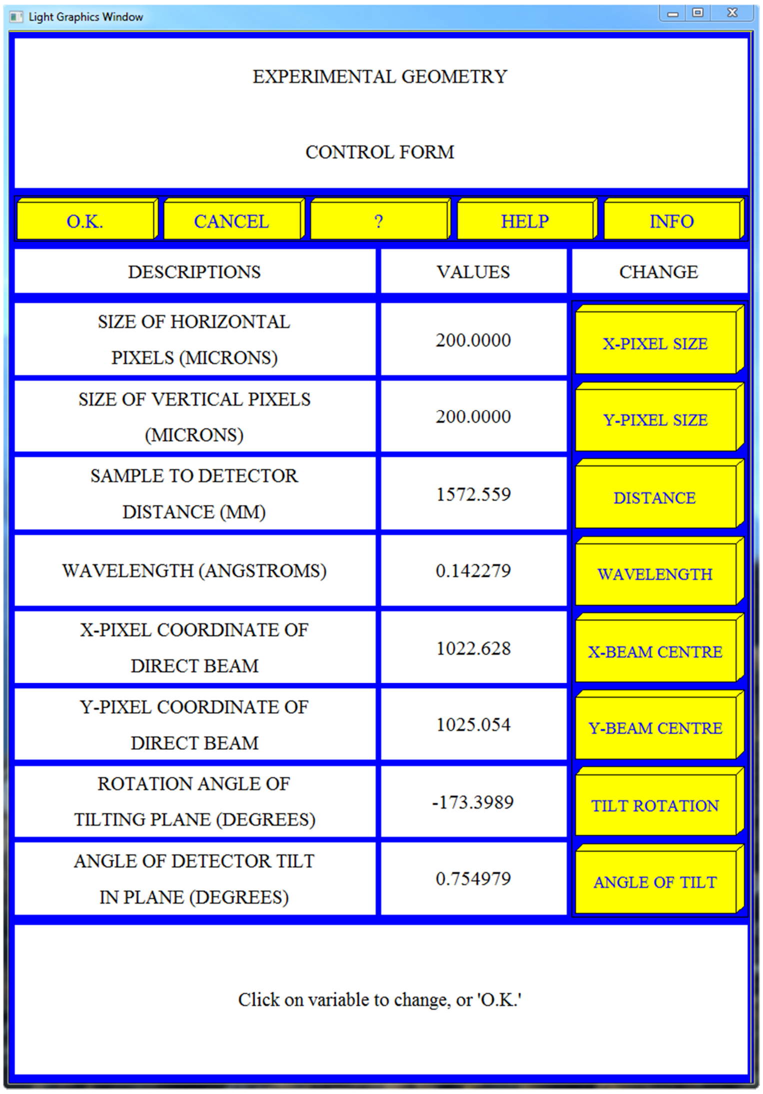

EXPERIMENTAL GEOMETRY

CONTROL FORM

DESCRIPTIONS	VALUES	CHANGE
SIZE OF HORIZONTAL PIXELS (MICRONS)	200.0000	X-PIXEL SIZE
SIZE OF VERTICAL PIXELS (MICRONS)	200.0000	Y-PIXEL SIZE
SAMPLE TO DETECTOR DISTANCE (MM)	1572.559	DISTANCE
WAVELENGTH (ANGSTROMS)	0.142279	WAVELENGTH
X-PIXEL COORDINATE OF DIRECT BEAM	1022.628	X-BEAM CENTRE
Y-PIXEL COORDINATE OF DIRECT BEAM	1025.054	Y-BEAM CENTRE
ROTATION ANGLE OF TILTING PLANE (DEGREES)	-173.3989	TILT ROTATION
ANGLE OF DETECTOR TILT IN PLANE (DEGREES)	0.754979	ANGLE OF TILT

Click on variable to change, or 'O.K.'

Figure 35. Parameters describing the geometrical arrangement of the sample, detector, and beam wavelength.

4.2.3 XRD peak fitting method

A diffraction image of a Bi-2212 wire recorded with the two dimensional detector is shown in Figure 36. The dark areas are those that have been covered with lead absorbers in order to prevent the diffracted signal of the sapphire single crystal tube from reaching the detector.

For the determination of the Ag lattice constants three high intensive Ag peaks (Ag(111), Ag(200), Ag(220)), whose diffraction rings are shown in Figure 36, are analysed further below.

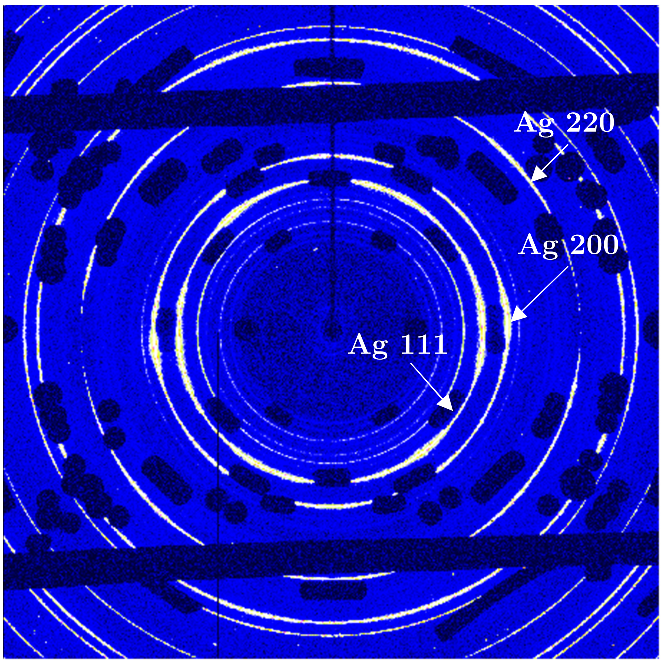

Figure 36. Diffraction image of a Bi-2212 wire.

The diffraction image is radially integrated around the transmitted X-ray beam centre in order to obtain the intensity vs d-spacing diffractogram as shown in Figure 37. The Ag diffraction peaks, with relatively high intensity, are labelled.

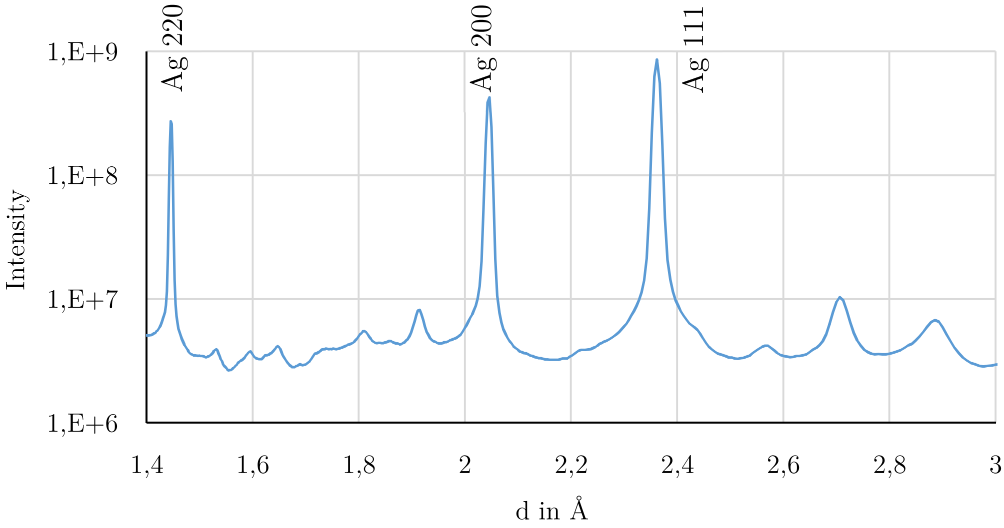

Figure 37. Integrated diffractogram of a Bi-2212 wire.

In order to measure the relative d-spacing changes the diffraction peaks have been fitted with Gaussian curves using the least square method. An example of a Ag peak with a Gaussian fit is shown in Figure 38. It can be seen that the Gaussian function fits the nearly symmetric Ag peak well.

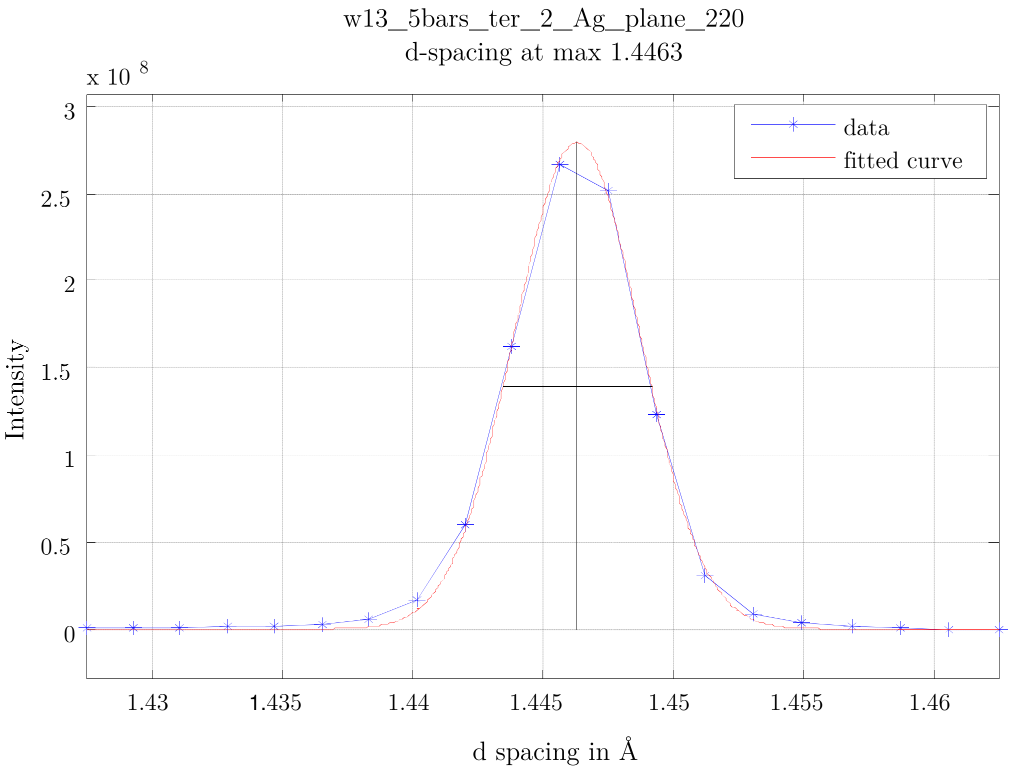

Figure 38. Fitted peak with the Gaussian curve using MATLAB.

More than 1000 diffractograms have been investigated. For each of these the intensive peaks of the planes 111, 200, 220 needed to be fitted, and therefore it was important to use an automatic and efficient procedure. For this purpose a MATLAB script, which is presented in the appendix, has been developed.

For the automatic fit of the individual peaks the program needs as an input the approximate d-spacing value related to each plane. Since the d-spacing increases with increasing temperature, the input of the temperature of each acquisition is also required. The temperature dependent d-spacings are then roughly pre-determined assuming a linear relationship between the temperature and the Ag lattice parameter. For an exact determination of the d-spacing the script fits a pre-defined number of data points that are distributed around the roughly pre-determined d-spacing value with a Gaussian curve using the least square method.

4.2.4 Temperature dependent Ag lattice parameter

The most intense peaks in the Bi-2212 wire diffractograms are the Ag peaks matrix and outer sheath. Assuming that the Ag in the wires does not change its composition during the HTs, the Ag lattice parameter increases with increasing temperature and can be used for a rough estimation of the sample temperature.

Ag and Bi-2212 d-spacing results of *ex situ* experiments

At the beginning of the beamtime MA2311 the diffraction pattern of three *ex situ* processed Bi-2212 wires have been acquired at RT. These samples have been processed by NHMFL-ASC. One sample was quenched from a peak temperature (T_{max}) of 500 °C, the second from T_{max}=821 °C, and the third sample was fully processed (T_{max}=888 °C) [14]. The d-spacing values determined for the most intense Ag and Bi-2212 peaks are summarised in Table 8.

Table 8. Ag and Bi-2212 d-spacing values determined for the three ex situ processed Bi-2212 wires.

Sample	*w13_ 500 °C*	*w13_ 821 °C*	*w13_888 °C*
d Ag (111) in Å	2.3611	2.3617	2.3610
d Ag (200) in Å	2.0445	2.0457	2.0445
d Ag (220) in Å	1.4458	1.4458	1.4457
d Bi-2212 (115) in Å	3.2493	3.2484	3.2489
d Bi-2212 (002) in Å	15.292	15.375	15.326
d Bi-2212 (113) in Å	3.5879	3.5799	3.5801

Ag has a face centred cubic lattice with a lattice constant of a=4.085 Å at ambient temperature [33]. The corresponding d-spacings reported for pure Ag at ambient temperature are d-Ag(111)=2.3587 Å, d-Ag(200)=2.0427 Å and d-Ag(220)=1.4444 Å [33].

Assuming that the Ag lattice parameter is not modified by the different HTs, the small d-spacing variations between the different samples show the influence of experimental uncertainties on the d-spacing results. Errors can come, for instance, from sample alignment and calibration of the beam wavelength, beam centre position and peak fitting. The Ag d-spacings measured during the MA 2311 *ex situ* experiments at ESRF at RT using the different Bi-2212/Ag wires varied by about ±0.06% (±one standard deviation).

The Ag sheath of the wires is alloyed with 0.2 wt% Mg, and the wire matrix consists of pure Ag. In the present experiment these two parts cannot be distinguished, and therefore, the Mg alloying of the sheath can have a small influence on the Ag d-spacing results. XRD results of the *in situ* experiments.

Lattice parameter results of the *in situ* experiments

In addition to the aforementioned *in situ* experiments that were performed during the beamtime MA2311 in November 2014, three more previous experiments have been investigated and are presented below.

The 'Bi_100bars-air' heat cycle was performed in air at 100 bar total pressure inside the high pressure cell in October 2011. The cycle 'Bi2212_25btot' was performed in air at 25 bar total pressure in December 2013. The heat cycle 'Bi-2212-w13-high-res-air' was performed in ambient air in the ID15A tomography furnace in April 2011. The 'Bi-2212-w13-high-res-air' experiment has been set-up for high resolution XRD measurements using a calibrated S-type thermocouple spot welded onto the sample. The XRD results of this experiment are used here as a reference data set to which the less accurate XRD experiments, performed with the sample inside the high pressure cell, can be compared.

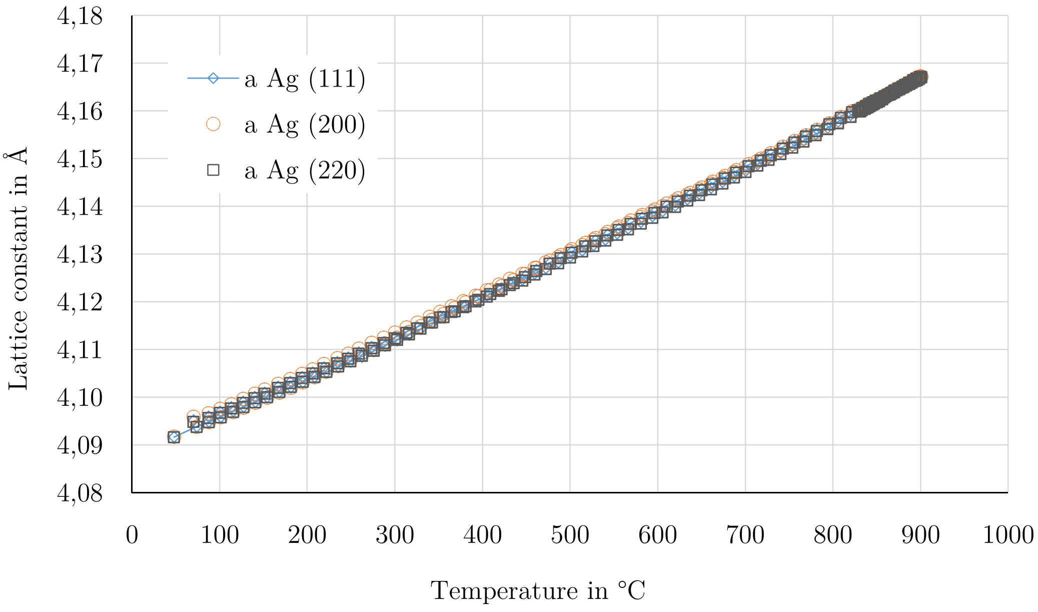

Figure 39. Comparison of the Ag lattice parameter calculated from the Ag(111), Ag(200) and Ag(220) d-spacing as a function of temperature (Bi-2212-w13-high-res-air).

The Ag lattice constants were calculated from the Ag(111), Ag(200) and Ag(220) d-spacing values using Equation 2.3.

Figure 39 compares the Ag lattice parameters calculated from three Ag diffraction peaks acquired during the 'Bi-2212-w13-high-res-air' experiment. It can be seen that the lattice parameter results are nearly identical, regardless of the diffraction peak from which they have been calculated. Thus, in the following, only the average of the three calculated lattice parameter values is presented.

The Ag lattice parameter changes recorded during heating up and cool down during 'Bi-2212-w13-high-res-air' are compared in Figure 40. It can be seen that a nearly identical temperature-lattice parameter relationship is obtained for the different temperature ramps.

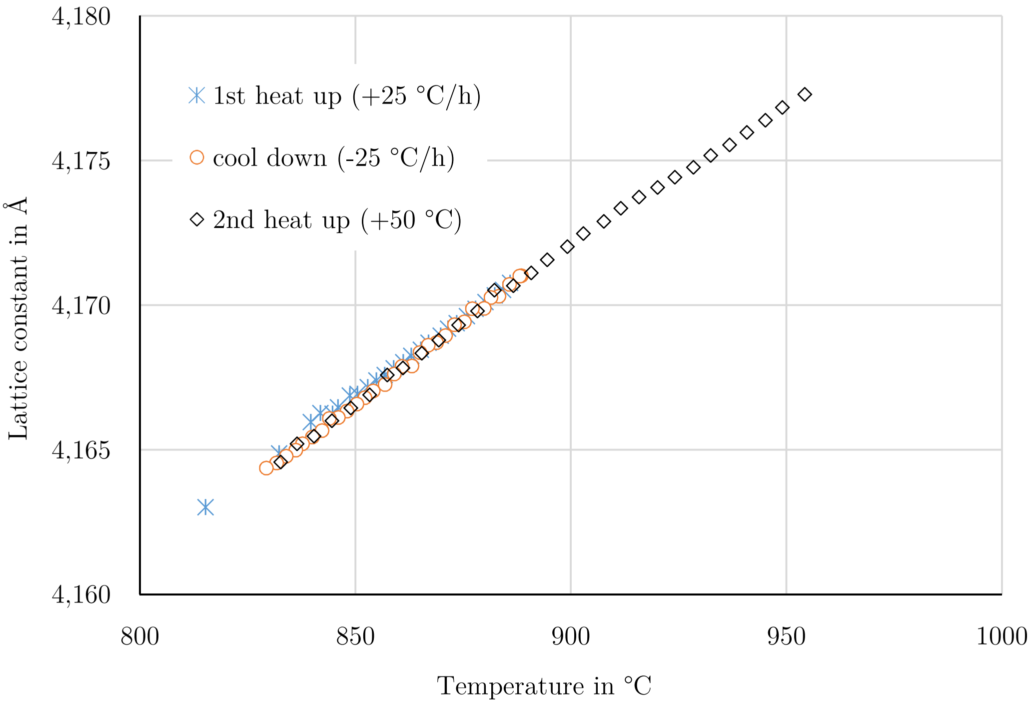

Figure 40. Comparison of the Ag lattice parameter calculated from the average Ag (111), Ag (200) and Ag (220) d-spacing as a function of temperature during heat up and cool down (Bi-2212-w13-high-res-air).

In Figure 41 previously recorded Ag lattice parameter vs temperature results (experiment 'Bi2212_25tot') are compared with the 'Bi-2212-w13-high-res-air' lattice parameter temperature dependence. Experiment 'Bi2212_25tot' was performed using a self-made non-calibrated thermocouple. From the temperature calibration of a self-made thermocouple it is estimated that the correct sample temperature is about 7% lower than the temperature reading during the experiment ‘Bi2212_25tot’ [34].

By comparing the slopes of the reference curve ‘Bi-2212-w13-high-res-air’ with the one of ‘Bi2212_25tot’ it can be estimated that the true temperature has to be about 7.3% lower than the self-made thermocouple temperature reading (using linear fits in the temperature range from 20 to 750 °C).

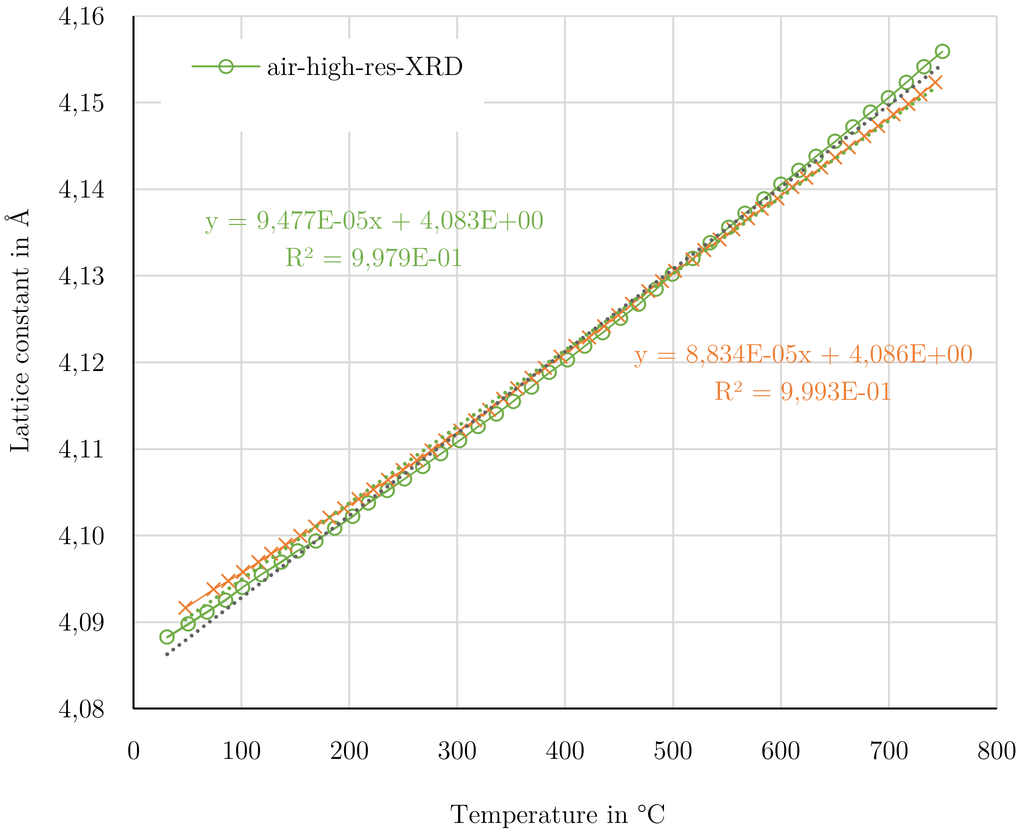

Figure 41. Comparison of the Ag lattice parameter temperature dependence measured at ESRF ID15 Bi-2212-w13-high-res-air with Bi-2212_25tot.

In Figure 42 the temperature dependent Ag lattice parameters determined from the XRD data of different *in situ* heat cycles are compared. It can be seen that the Ag lattice constants increase approximately linearly as a function of the temperature. They differ in slope and offset from the reference 'Bi-2212-w13-high-res-air' sample. The 'Bi_100bars_air' sample has a huge lattice parameter offset as compared to the other data sets.

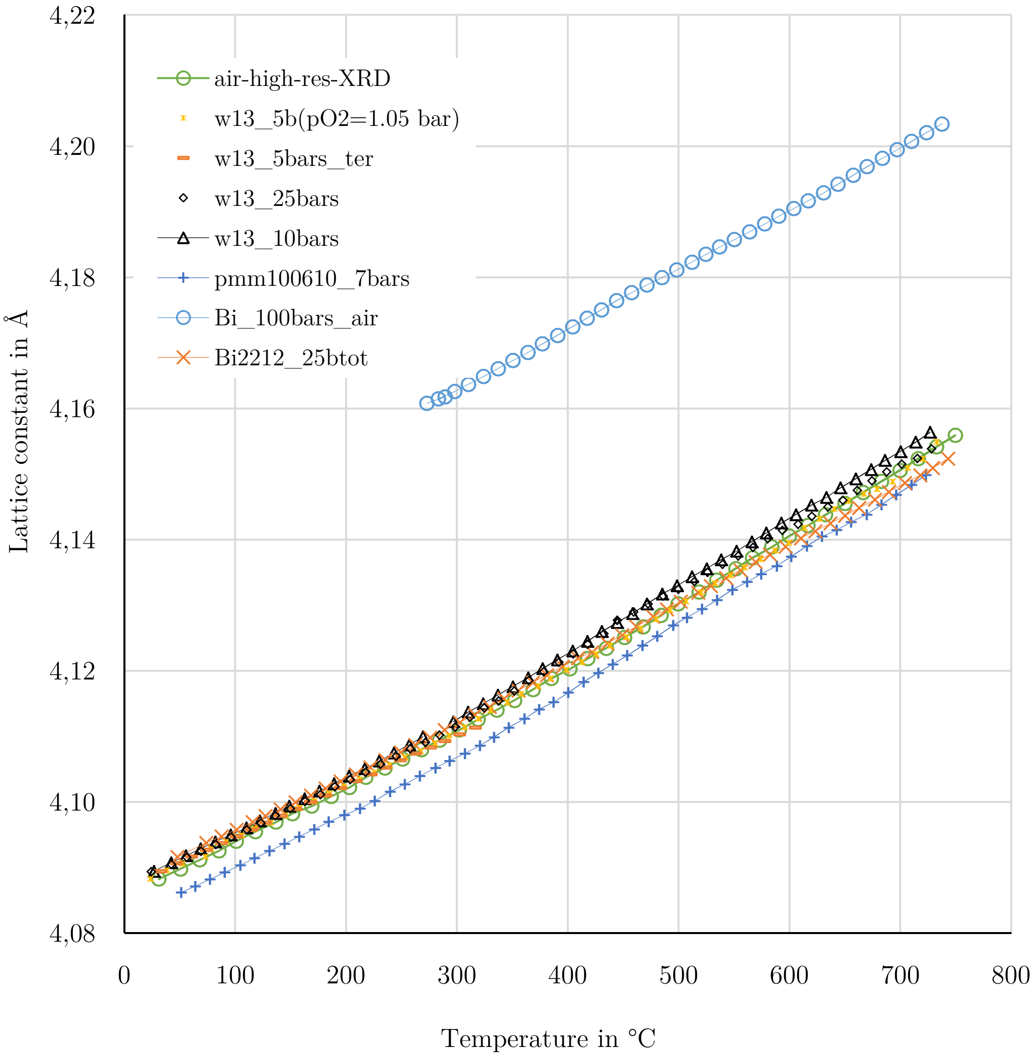

Figure 42. Comparison of the temperature dependent Ag lattice parameter determined from the XRD data of different in situ heat cycles at ESRF ID15B.

Figure 43 compares the fluctuation of the Ag lattice constant during long, constant temperature plateaus of 832 °C. The maximum variation of the temperature measured with the thermocouple during these plateaus was ±0.7 °C. It can be seen in Figure 43 that despite the negligible temperature variations that are measured with the thermocouple the lattice constant calculated from the Ag d-spacing fluctuates rather strongly up to ±0.0013 Å.

The apparent Ag lattice parameter variations observed during heat cycle 'pmm100610_7bar' would correspond either to temperature fluctuations of ±13 °C, or variations of the sample-to-detector distance of ±0.9 mm.

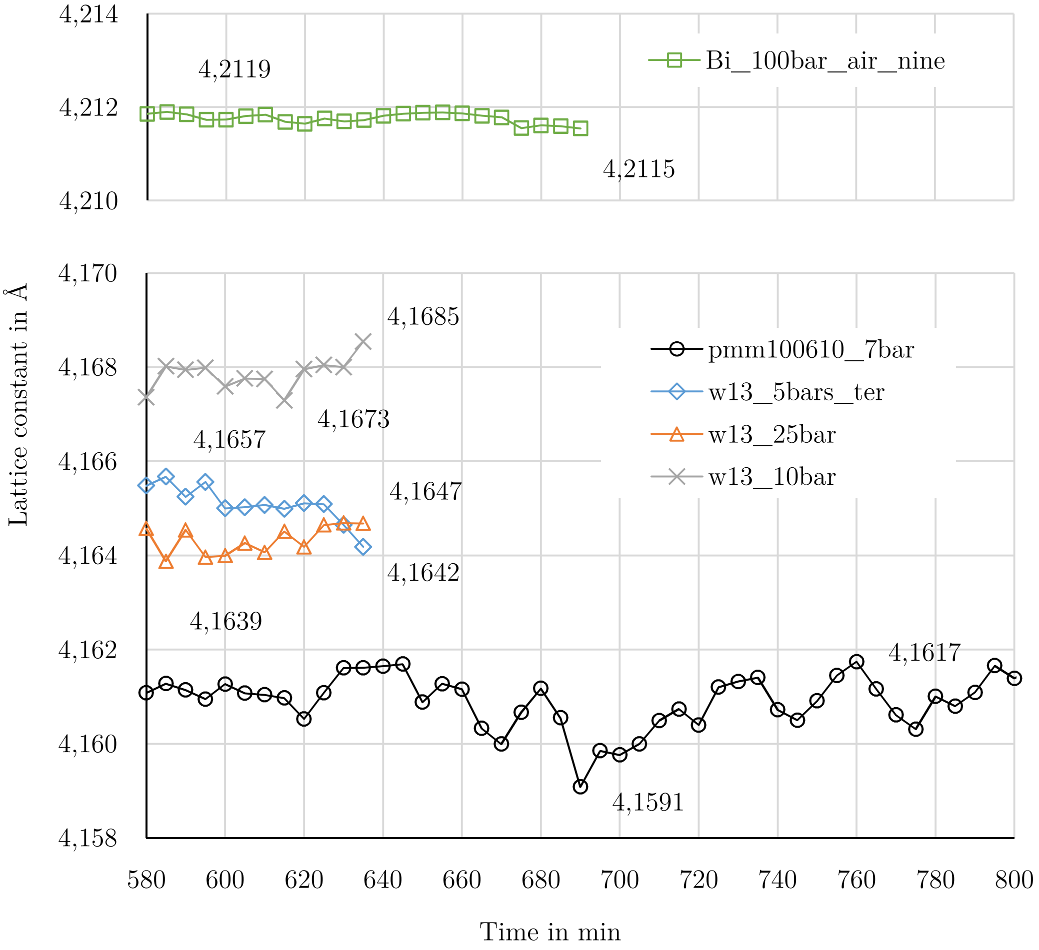

Figure 43. Change of the Ag lattice constant at constant thermocouple temperature reading of 832±0.7 °C.

4.3 Metallographic examination of Bi-2212 wires

The microstructure of the Bi-2212 wire after two different HTs was characterised by optical metallography. The HTs were performed with the tube furnace at CERN at ambient pressure using the sample holder shown in Figure 12 and a type K thermocouple. The samples were heated up with a ramp rate of 160 °C/h to a peak temperature. One sample was heated up to 830 °C and the other sample to 888 °C. After a 5 min plateau at the peak temperature the furnace was turned off and the sample was quenched in ambient air.

For the mechanical grinding and polishing the heat treated Bi-2212 wires were embedded in a resin. These samples were then grinded with refined abrasive papers and water. For the final polishing step a diamond suspension with 9 µm particles was used.

Micrographs after HT in ambient air

The optical micrographs of the Bi-2212 wire after HT to a maximum temperature of 888 °C at ambient pressure are shown in Figure 44. It can be clearly observed that the shape of the filaments has strongly changed in comparison to the beginning (see Figure 4).

Before the HT was performed the filament boundaries were well separated. Most of the filaments had their own defined position in the Ag matrix. After the HT parts of the filaments crossed the Ag matrix and connected two or more filaments. Also many different shades appeared in the filaments so there might be more, different phases.

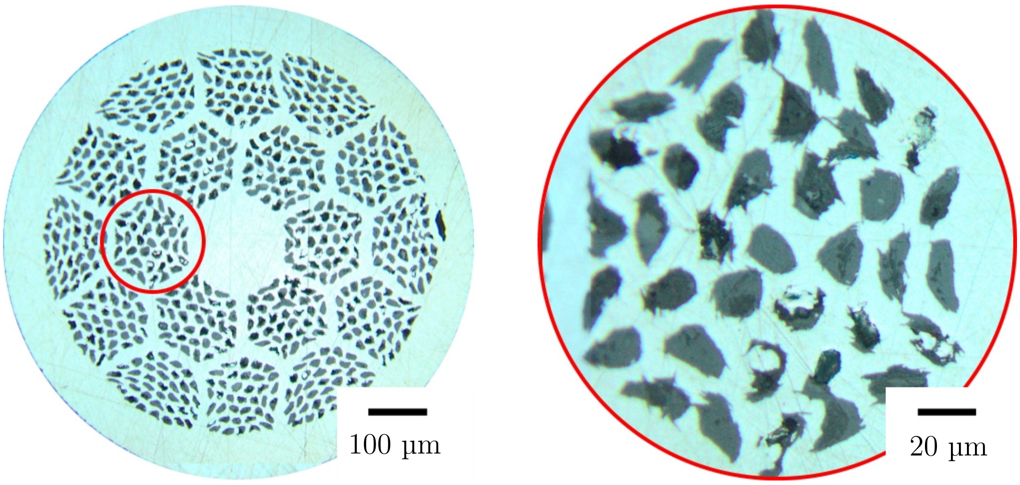

Figure 44. Cross section of the Bi-2212 sample after heating 160 °C/h to T_{max}*=888 °C in ambient air.*

The cross section from the other sample, which only reached a maximum temperature of 830 °C, is shown in Figure 45. The shape of the filaments here is more similar to the original wire (see Figure 4). However, the boundaries between the filaments and the Ag matrix seem to be a little bit smoother after this HT. Also some small spots can be discovered in the filaments. This could be an evidence of a first phase change of the Bi-2212 powder.

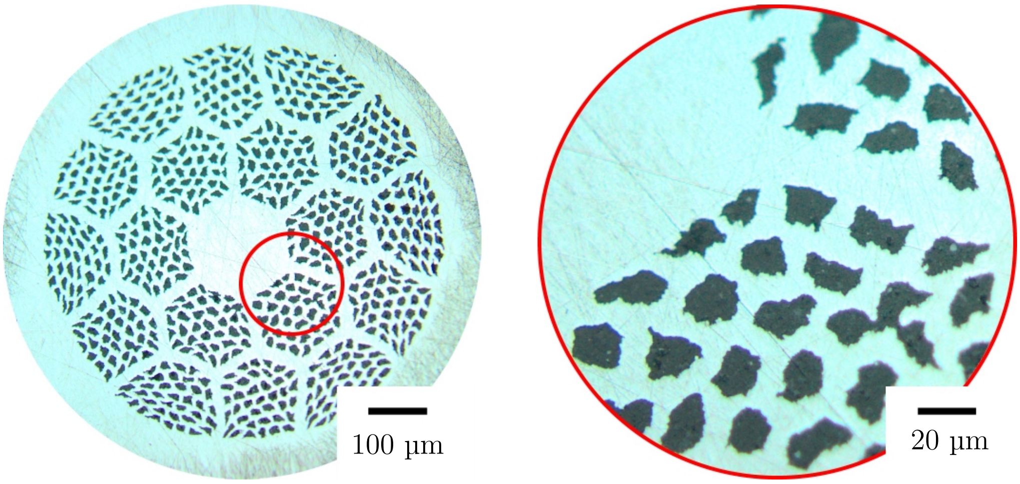

Figure 45. Cross section of the Bi-2212 sample after heating 160 °C/h to T_{max}*=830 °C in ambient air.*

5 Discussion and conclusion

The two main subjects of this thesis were the setting up of a high pressure furnace for the processing of Bi-2212 wires and the analysis of XRD data acquired during *in situ* studies of the phase changes occurring during the Bi-2212 wire processing that were performed at the ID15 beamline of the ESRF.

5.1 The OP furnace pressure and temperature control

The OP furnace that is set up at CERN is loosely based on the design of the OP furnace used at the ID15 beamline for the *in situ* XRD studies. It is a tube furnace in which the extremities of the high pressure cell should remain below 200 °C when the centre of the cell is heated to the maximum temperature of 888 °C.

The temperature profile along the ends of the high pressure cell has been measured during a HT to a peak temperature of 888 °C in the centre of the cell. It can be seen in Figure 16 that the maximum temperature measured at the tube ends is about 170 °C, which is compatible with the use of Swagelok fittings.

The diameter at the ends of the Hastelloy X-750 tube has been reduced to 25 mm, which is compatible with the use of Swagelok fittings SS-25-M0-6-18, which connect the pressure controller, leak valve and a thermocouple to the high pressure cell. The high pressure cell and the fittings have been tested up to a pressure of 250 bar. After the pressure was held for one hour no leakage was noted.

All hardware components needed for the pressure and temperature control of the furnace have been selected in collaboration with the CERN LabVIEW team. They were interconnected and mounted in a switchboard, and connected to the pressure controller and the temperature sensor. To control the pressure in the OP furnace and to log the data of the sample temperature a LabVIEW program was developed.

5.2 Estimation of the sample temperature from the Ag d-spacing

The second main subject of this thesis was the analysis of the XRD data that has been acquired during various *in situ* XRD studies of the phase changes in Bi-2212 wires at the ID15 beamline of ESRF.

In particular the temperature dependent lattice parameter changes of the Ag matrix of the Bi-2212 wires were determined from the XRD data in order to cross-check the temperature readings with the thermocouples that were spot welded onto the wires. In addition to the XRD data acquired during the beamtime MA2311, data sets from previous beamtimes have also been analysed and compared with each other (see 4.2.4).

A summary of the Ag lattice parameters determined from the different XRD data sets is presented inTable 9. For this comparison the lattice parameter vs temperature curves, shown in Figure 42, have been fitted with linear functions. The apparent Ag lattice parameters at 0 °C were determined from these fits.

By comparing the different slopes of lattice parameter vs temperature with the reference data set 'Bi-2212-w13-high-res-air', an error in the different thermocouple temperature measurements has been estimated. A strong temperature error is found for the data sets 'Bi2212_25tot' and 'Bi_100bars-air'. Both experiments have been performed with a self-made non-calibrated thermocouple.

The results presented in Table 9 confirm the important error in the temperature reading of these thermocouples, and allow for a correction of the errors. For the experiments using commercial calibrated S-type thermocouples the temperature errors are smaller than 10 °C.

Table 9. Ag lattice parameter at 0 °C and the linear slope of the lattice parameter vs temperature in the range from 270 °C to 740 °C. The temperature deviation is calculated by comparing the slope with that of the reference data set 'Bi-2212-w13-high-res-air'.

Sample name	*a at 0 °C in Å*	*Slope ×10^{-5} in Å/K*	*R-squared*	*T deviation in K*
Bi-2212-w13-high-res-air	4.080	10.03	0.9995	0.0
Bi2212_25btot	4.085	9.090	0.9999	44
W13_5b(pO2=1.05 bar)	4.081	9.892	0.9990	6.0
W13_25bars	4.083	9.821	0.9987	9.3
W13_10bars	4.082	10.22	0.9999	-9.4
Pmm100610_7bars	4.076	10.14	0.9997	-5.6
Bi_100bars-air	4.135	9.184	0.9998	39

While the slope of the Ag lattice parameter vs temperature curves allows for a rough estimate of the thermocouple temperature error, the strong deviations of the absolute lattice parameters at a certain temperature cannot be explained by temperature uncertainties only. Other experimental uncertainties that limit the accuracy of the absolute Ag lattice constant measurements include the energy calibration, uncertainties in the sample alignment and the sample-to-detector distance, the radial integration peak fitting errors, the influence of alloying elements and impurities in the reference materials (silver).

The d-spacing error as a function of sample-to-detector distance error is shown in Table 7. The d-spacing error increases linearly with the sample-to-detector distance error, and a 1 mm error of the sample-to-detector distance causes an approximate d-spacing error of 0.06%. Apart from the sample 'Bi_100bars-air' the 0 °C lattice parameter differences shown in Table 9 could be explained by sample-to-detector distance uncertainties of up to 2 mm.

Only a huge error in the sample-to-detector distance and/or the energy calibration can explain the extreme 0 °C Ag lattice parameter error of about 1.3% found for sample 'Bi_100bars-air' (see Figure 42).

REFERENCES

[1] CERN. (2014, April) About Cern. [Online]. http://home.web.cern.ch/about

[2] CERN. (2015, February) Technology Department. [Online]. http://te-dep.web.cern.ch/content/organization

[3] CERN. (2015, January) Technology Department. [Online]. http://te-dep.web.cern.ch/content/magnets-superconductors-and-cryostats-msc

[4] CERN. (2015, March) The Large Hadron Collider. [Online]. http://home.web.cern.ch/topics/large-hadron-collider

[5] J.L Caron. (1998 , May) Cross section of LHC dipole. [Online]. http://cds.cern.ch/record/841540

[6] L. Evans, P. Bryant, "The CERN large hadron collider: accelerator and experiments," JINST 3 S08001, Geneva, 2008.

[7] CERN. (2015, February) The FCC-ee design study. [Online]. http://tlep.web.cern.ch/

[8] P.J. Lee, "Superconductor: Wires and cables: Materials and processes," The Applied Superconductivity Center, The University of Wisconsin-Madison, 2002.

[9] J. Emanuelson, S. Pike. (1998) Resistance vs. temperature in a superconducting YBCO bar. [Online]. http://www.futurescience.com/manual/sc500.html

[10] Scott Technology NZ Limited (2014). Cryogen-free compact MRI systems. [Online]. http://www.hts110.co.nz/magnetic-resonance/mri/

[11] D.C. Larbalestier, J. Jiang, U.P. Trociewitz, F. Kametani, C. Scheuerlein, M. Dalban-Canassy, M. Matras, P. Chen, N.C. Craig, P.J. Lee, E.E. Hellstrom, "Isotropic round wire multifilament cuprate superconductor for generation of magnetic fields above 30 T," Nature Materials, Vol. 13, doi:10.1038/nmat3887, 2014.

[12] B. Heeb, "Das Schmelzprozessieren von massivem $Bi_2Sr_2CaCu_2Ox$ (Bi-2212)," PhD thesis, ETH Zürich, 1993.

[13] C. Scheuerlein, M. Di Michiel, M. Scheel, J. Jiang, F. Kametani, A. Malagoli, E.E. Hellstrom, D.C. Larbalestier “Void and phase evolution during the processing of Bi-2212 superconducting wires monitored by combined fast synchrotron micro-tomography and x-ray diffraction,” Supercond. Sci. Technol. 24, 115004, 2011.

[14] J. Jiang, W. L. Starch, M. Hannion, F. Kametani, U. P. Trociewitz, E. E. Hellstrom, D. C. Larbalestier, “Doubled critical current density in Bi-2212 round wires by reduction of the residual bubble density,” Supercond. Sci. Technol. 24, 082001, 2011.

[15] ESRF. (2014) ID15 - High Energy Scattering Beamline. [Online]. http://www.esrf.eu/UsersAndScience/Experiments/StructMaterials/ID15

[16] M. Zinser, C. Scheuerlein, “A furnace for the overpressure processing of Bi-2212/Ag high temperature superconducting wires,” CERN, TE-MSC, Geneva, 2014.

[17] Swagelok Company, “An Installer’s Pocket Guide for Swagelok Tube Fittings,” R9 MS-13-151, 2014.

[18] Swagelok Company, “Stainless Steel Seamless Tubing,” R1 MS-01-181, 2014.

[19] Inc Haynes International, “HAYNES® X-750 alloy,” Kokomo, 2008.

[20] G. Holzmann, H. Meyer, G. Schumpich, “Technische Mechanik Festigkeitslehre,” Vieweg + Teubner Verlag, 9. Auflage, 2006.

[21] Swagelok Company, “Tensile Pull Test of 316 Stainless Steel Swagelok,” Solon (Ohio), PTR-1193 Rev. C, 2012.

[22] D.P. Gonnard, “Inspection de Sécurité Réception sur CRPEMS-00270 (Epuipements Mecaniques Speciaux),” CERN, EDMS No. 1464670, 2015.

[23] National Instruments, “Operating instructions and specifications / NI 9214 with NI TB-9214,” 375138B-01, 2010.

[24] Bronkhorst High-Tech, “El Press Hook-up diagram - Analog I/O + RS232,” doc. nr.: 9.18.062, Ruurlo, 2011.

[25] National Instruments, “NI cRIO Instructions,” 376257A-01, 2014.

[26] Bronkhorst High-Tech, "Operational Instructions for digital Multibus Mass Flow / Pressure instruments," Ruurlo, Doc. no.: 9.17.023AC, 2014.

[27] Bronkhorst High-Tech, "Instruction manual FlowDDE," Ruurlo, 9.17.067, 2011.

[28] Bronkhorst High-Tech. (2014, July) Certified LabVIEW Plug and Play (project-style) Instrument Driver. [Online]. http://www.bronkhorst.com/en/downloads/labview

[29] J. Andrieux, C. Chabert, A. Mauro, H. Vitoux, B. Gorges, T. Buslaps, V. Honkimäki, "A high pressure and high temperature gas loading system for the study of conventional to real industrial sized samples in catalyzed gas/solid and liquid/solid reactions," J. Appl. Cryst. 47, doi:10.1107/ S1600576713030197, 2014.

[30] ESRF. (2014) High temperature gas loading system for catalyzed gas/solid or liquid/solid reactions. [Online]. http://www.esrf.eu/UsersAndScience/Experiments/StructMaterials/ID15/Technical_overview/high-temperature-gas-loading-system-for-catalyzed-gas-solid-or-liquid-solid-reactions

[31] NIST. (2012, March) Material Details - SRM 674b - X-Ray Powder Diffraction Intensity Set (Quantitative Powder Diffraction Standard). [Online]. https://www-s.nist.gov/srmors/view_detail.cfm?srm=674B

[32] A. Hammersley. (2004, November) The fit2d home page. [Online]. http://www.esrf.eu/computing/scientific/FIT2D/

[33] J. Spreadborough, J.W. Christian, "High-temperature X-ray diffractometer," J. Sci. Instrum. 36 116., doi:10.1088/0950-7671/36/3/302, 1959.

[34] C. Scheuerlein, "Visit Report," CERN, EDMS No. 1312609, 2013.

A MATLAB SCRIPT

Initial

```
%%%%%%%%%%%%%%%%%%%%%%%%%%%%%%%%%%%%%%%%%%%%%%%%%%%%%%%%%%%%%%%%%%%%%%%%%%%%%
%%%%%% Project: Automatic Peak fitting for in situ diffractograms      %%%%%%
%%%%%% Autor:   Christopher Doerrer                                    %%%%%%
%%%%%% Date:    12/03/2015                                             %%%%%%
%%%%%% Group:   CERN TE-MSC                                            %%%%%%
%%%%%%%%%%%%%%%%%%%%%%%%%%%%%%%%%%%%%%%%%%%%%%%%%%%%%%%%%%%%%%%%%%%%%%%%%%%%%

set(0, 'DefaulttextInterpreter', 'none')
close all; clear all;
```

Declarations

```
expname = 'w13_pmm100610_7bars';    % name of the experiment folder
addpath(expname);                   % search also in that folder

est(1,1) = 111;                     % Ag planes that shall be fitted
est(1,2) = 200;
est(1,3) = 220;

aconstant = 4.086;                  % a at 0 degrees Celsius in Angstrom
slope = 9.41e-5;                    % slope in Angstrom per Kelvin

qdis = 0.05547063400;               % distance between data points of
                                    % diffractogram, approximately constant

pointnum = 30;                      % number of points that shall
                                    % be included for the fitting

mkdir([expname '_results']);        % create new folder for results
addpath([expname '_results']);      % add folder

firstfile = 2;                      % first file number example 0003 -> 3
lastfile = 4;                       % last file number example 0149 -> 149

expinfo = importdata(['/', expname,'/',expname, '.info'],' ',0);
                                    % get info file of the experiment
res(:,1) = expinfo(1,1).data(:,6);  % save temp in results
a0 = [0, 0, 0];                     % preallocating vector
alld = struct('data',nan(1450,2),'textdata',cell(1,lastfile));
                                    % preallocating structure
fitv = nan(pointnum,2);             % preallocating matrix
```

Get all diffraction data and calculate estimated d-spacings

```
for i0 = firstfile:1:lastfile

    if i0 > 99 && i0 < 1000         % if file ending is in this range
        file = [expname '_0' int2str(i0) '.dat'];   % opening the data files
    elseif i0 > 9 && i0 < 100
        file = [expname '_00' int2str(i0) '.dat'];  % opening the data files
    elseif i0 > 0 && i0 < 10
        file = [expname '_000' int2str(i0) '.dat']; % opening the data files
    end

    for i1=1:1:3
    miller = sprintf('%d',est(1,i1)) - '0';
                                    % getting the miller indices from 1 cell
                                    % into a vector
    est(i0+1,i1)= 20*pi/((aconstant+slope*expinfo(1,1).data(i0,6))/norm(miller));
                                    % calculating all d-sapcings and
                                    % converting to q in nm
    end

    alld(i0) = importdata(file,' ',4);
end
```

Start Fitting

```
for i0 = firstfile:1:lastfile

        for i1 = 1:1:3               % 3 fittings for every file

        h = figure('visible','off'); % do not open figure

        bord(1) = est(i0+1,i1) - pointnum*qdis/2; % calculate the border
        bord(2) = est(i0+1,i1) + pointnum*qdis/2; % for the points to be fitted

        z = 1;                      % line for fitting matrix, start with 1
        for i2 = 1:1:1449           % for every line of the file

            if  alld(i0).data(i2,1) > bord(1) && alld(i0).data(i2,1) < bord(2)
                                    % if a value is between the border
                fitv(z,:) = alld(i0).data(i2,:);
                                    % write the points to be fitted in fitting
                z = z+1;            % increase line for fitting
            end
        end

        fitv(:,1) = (20*pi)./fitv(:,1);    % from Q in nm to dspacing in Angs
        fitv(:,2) = fitv(:,2)-(fitv(1,2)+fitv(pointnum,2))/2;
        f = fit(fitv(:,1),fitv(:,2),'gauss1');    % doing the Gauss fitting
```

```
        C = coeffvalues(f);         % resulsts from the fitting
        dsp = C(2);                 % calculating the d spacing
        miller = sprintf('%d',est(1,i1)) - '0';
                                    % getting the miller indices from 1 cell
        a0(i1) = dsp*norm(miller);  % calculating lattice constant

        plot(f,fitv(:,1),fitv(:,2),'*-');         % connect points with line
        axis([fitv(pointnum,1), fitv(1,1), fitv(1,1)-C(1)/10, C(1)+C(1)/10]);
                                    % fit figure in the centre
        grid on;                    % make grid visible in plot
        xlabel('d spacing in Å');   % axis names
        ylabel('Intensity');

        line([dsp dsp], [0 C(1)],'color','k');    % verticel line
        width = 5/3*C(3);           % width at half of the maximum intensity

        line([(dsp-width/2) (dsp+width/2)], [C(1)/2 C(1)/2],'color','k');
                                    % horizontal line

        name = [expname '_' num2str(i0) '_Ag_plane_' num2str(est(1, i1))];
                                    % create name for the 3 fittings
        title({name; ['d-spacing at max ',num2str(dsp)]});

        saveas(h,[expname '_results/' name], 'png');   % Save as png

        res(i0,i1+1) = dsp;
        res(i0,i1+4) = a0(i1);

    end
    res(i0,8) = mean(a0);           % average of the lattice constant
    if i0>1
        l0 = res(i0-1, 8);          % initial length
        l1 = res(i0,8);
        res(i0,9) = 1/l0*(l1-l0)/(res(i0-1,1)-res(i0,1));
                                    % thermal expansion coefficient
    end
end
```

Save to file

```
xlswrite([expname '_results'],res); % write the result file
```

Published with MATLAB® R2014a